BACE1 in PV interneuron tunes hippocampal CA1 local circuits and resets priming of fear memory extinction

Yan Zheng (zhengyan@ccmu.edu.cn)
Capital Medical University https://orcid.org/0000-0002-0864-069X
Xuansheng Xiao
Xiaotong Wang
Ke Zhu
Lijuan Li
Ying He
Jinglan Zhang
Hanning Hu
Yanqiu Cui
Jianliang Zhang

Article

Keywords:

Posted Date: October 6th, 2022

DOI: https://doi.org/10.21203/rs.3.rs-2017936/v1

Version of Record: A version of this preprint was published at Molecular Psychiatry on July 14th, 2023.
See the published version at https://doi.org/10.1038/s41380-023-02176-y.

Abstract

BACE1 is the rate-limiting enzyme for β-amyloid (Aβ) production and therefore is considered a prime drug target for treating Alzheimer's disease (AD). Nevertheless, the BACE1 inhibitors failed in clinical trials, even exhibiting cognitive worsening, implying that BACE1 may function in regulating cognition-relevant neural circuits. Here, we found that parvalbumin-positive inhibitory interneurons (PV INs) in hippocampal CA1 express BACE1 at a high level. We designed and developed a mouse strain with conditional knockout of BACE1 in PV neurons. The CA1 fast-spiking PV INs with BACE1 deletion exhibited an enhanced response of postsynaptic N-methyl-D-aspartate (NMDA) receptors to local stimulation on CA1 oriens, with average intrinsic electrical properties and fidelity in synaptic integration. Intriguingly, the BACE1 deletion reorganized the CA1 recurrent inhibitory motif assembled by the heterogeneous pyramidal neurons (PNs) and the adjacent fast-spiking PV INs from the superficial to the deep layer. Moreover, the conditional BACE1 deletion impaired the AMPARs-mediated excitatory transmission of deep CA1 PNs. Further rescue experiments confirmed that these phenotypes require the enzymatic activity of BACE1. Above all, the BACE1 deletion resets the priming of the fear memory extinction. Our findings suggest a neuron-specific working model of BACE1 in regulating learning and memory circuits. The study may provide a potential path of targeting BACE1 and NMDAR together to circumvent cognitive worsening due to a single application of BACE1 inhibitor in AD patients.

Introduction

Beta-site amyloid precursor protein (APP) cleaving enzyme 1(BACE1) has been well known as the rate-limiting enzyme for β-amyloid (Aβ) production from APP aspartic proteolysis since it was discovered in 1999 [1–5]. After that, BACE1 has been listed as a prime drug target for treating Alzheimer's disease (AD), the most common cause of dementia in older people [6, 7]. However, the BACE1 inhibitors entering clinical trials showed no cognitive or functional improvement, even exhibiting cognitive worsening [8]. The failure of therapeutic strategies targeting BACE1 in AD treatment calls for an enormous effort to elucidate a relatively straightforward role of BACE1 in the neural network associated with cognition.

With a high expression level in neurons, BACE1 is often located at synapses containing presynaptic and postsynaptic compartments [9–11]. BACE1 systemic knockout mouse was initially designed and developed to explore a strategy to reduce Aβ production [12]. However, subsequent findings revealed many phenotypes, such as central and peripheral hypomyelination [13, 14], synaptic dysfunction [15, 16], seizures [17, 18], schizophrenia-like behavior [19], and retinal pathology [20], in the BACE1 KO mice resulting from loss of function of substrates under BACE1 enzymatic activation. Most of these substrates, e.g., neuregulin1, SEZ6, CHL1, Neurexin 1α and 3β, have a hand in neuronal functions and synaptic transmission, partly explaining why BACE1 blockade caused a cognitive decline in AD patients [10]. In addition, BACE1 could regulate ion channels independent of its enzymatic activation [21]. The evidence suggests that BACE1 has a critical physiological role in the information coding process of neural networks. Nevertheless, the exact working model underlying BACE1 in regulating cognitive neuronal circuits needs a precise interpretation.

The diversity of neuronal populations makes it challenging to elucidate the complicated working model of neural networks. Thus, the unselected BACE1 knockout might cause inconsistency in those findings in different labs because of the above-intricated effects of BACE1. Here, we hypothesized that BACE1 might function in a neuron-specific manner in regulating the cognitive circuit. The immunostaining result of BACE1 co-expressing with parvalbumin-positive neurons (PV neurons) in mouse brains promoted us to design and develop a mouse strain with conditional knockout of BACE1 in PV neurons. The CA1 PV interneurons (PV INs) with BACE1 deletion exhibited an enhanced response of postsynaptic N-methyl-D-aspartate (NMDA) receptors to local stimulation on CA1 oriens, while with normal excitability, intrinsic electrical properties, and fidelity in synaptic integration. As a result, the homeostasis of excitatory/inhibitory synaptic transmission in the CA1 pyramidale was disrupted in a non-uniform manner. Eventually, the BACE1 deletion in CA1 PV INs retunes the CA1 pyramidal activity and resets the priming of fear memory extinction. Further rescue experiments confirmed that these phenotypes require the enzymatic activity of BACE1. Our findings suggest a neuron-specific working model of BACE1 in regulating learning and memory circuits. The study may provide a potential path of targeting BACE1 and NMDAR together to circumvent cognitive worsening due to a single application of BACE1 inhibitor in AD patients.

Results

Conditional BACE1 deletion did not change the electrophysiological properties of CA1 PV INs

Although BACE1 was found mainly in neurons, its neuron-type specific expression was unknown. Thus, immunofluorescent staining first detected the profile of BACE1 expression in the c57BL mouse brain. Consistent with the previous report, the BACE1 was dramatically concentrated in mossy fiber terminals [11, 22]. Most notably, we found a higher level of BACE1 in PV INs of the hippocampus, though it also occurred in other kinds of interneurons (Supplementary Fig. 3). PV INs contribute critical regulatory action to hippocampal networking by forming microcircuits with CA1 pyramidal neurons (PNs) and are involved in learning and memory [23]. The high expression of BACE1 in PV INs implied that BACE1 might regulate the function of PV INs in the hippocampal microcircuit.

To explore the role of BACE1 in the regulatory effect of CA1 PV INs in hippocampal microcircuit, we established a conditional knockout mouse carrying the *BACE1* mutant allele ($BACE1^{fl/fl}$ hereafter). In the strain, the exon 6–9 was flanked by *loxP* sites, and enhanced Green fluorescent protein (eGFP) was inserted as a reporter gene (Fig. 1A, Supplementary Fig. 1). Some neurons that look like interneurons segregated among CA1 PNs express a high level of GFP (Fig. 1B). We then co-labeled these neurons with anti-parvalbumin antibody (red, recognized by secondary antibody conjugated with Alexa fluor 594) and anti-BACE1 antibody (cyan, recognized by secondary antibody conjugated with Alexa fluor 647). As expected, most PV INs express BACE1 (Supplementary Fig. 4). Meanwhile, some interneurons were not parvalbumin-positive, despite with high level of BACE1 expression (Fig. 1D, Supplementary Fig. 4),

suggesting that the regulatory effect of BACE1 in the neural circuit is not confined to PV INs. Here, we crossed BACE1$^{fl/fl}$ line with the PV-Cre line to produce mice with BACE1-specific deletion in PV-positive neurons (BACE1$^{fl/fl}$;PV-Cre) (Fig. 1C) to investigate the role of BACE1 in the regulatory effect of PV INs in hippocampal CA1 microcircuit. As shown in Fig. 1D, PV INs surrounding the CA1 pyramidale layer displayed BACE1 negative. However, it should be noted that there were still some PV INs with no deletion of BACE1, implying that BACE1 expression may be prior to parvalbumin expression in these neurons, probably due to heterogeneity of development of PV INs [24]. Nevertheless, these neurons were distributed in areas far away from the CA1 pyramidale layer, excluding a possible interference to observation on the CA1 microcircuit regulated by basket PV INs. In the present study, we mainly focused on those perisomatic-targeting, fast-spiking basket PV INs in the CA1 pyramidale adjacent to stratum oriens.

To figure out whether BACE1 affects the electrophysiological properties of PV IN in CA1, we performed a whole-cell current-clamp recording. We used BACE1$^{fl/fl}$;Ai9;PV-Cre and Ai9;PV-Cre mouse slices to explore physiological changes of PV INs, which the fluorescent signal of Tdtomato can identify in a Cre recombinase-dependent manner [25]. As shown in Fig. 1E and 1F, we identified PV IN in CA1 stratum oriens (so) under a fluorescent microscope equipped with an electrophysiological recording setup and recorded it. First, BACE1 deletion did not change the action potential frequency of fast-spiking PV INs of BACE1$^{fl/fl}$;Ai9;PV-Cre mouse compared to that of Ai9;PV-Cre control (Fig. 1G, H) when a series of 500 ms suprathreshold step-current injections were applied. In addition, with the same resting membrane potential (Fig. 1I), BACE1 deletion did not alter the input resistance detected by 500 ms subthreshold step-current injections (Fig. 1J, K) in CA1 PV INs. Consistent with input resistance, the rheobase of CA1 PV INs evoked by a brief, 3 ms current injections was not altered by BACE1 deletion (Fig. 1L, M). Therefore, BACE1 deletion changed neither the intrinsic physiological properties nor the neuronal excitability of PV INs in the CA1 network. Moreover, we did not find any change in these electrical properties in CA1 PNs (Supplementary Fig. 5).

BACE1 deletion enhanced activity-dependent NMDAR responses in CA1 PV INs.

To explore whether the local excitatory synaptic inputs to PV INs were affected. We recorded evoked EPSCs, including AMPAR EPSCs and NMDAR EPSCs in PV INs with voltage-clamp configuration, while the stimulation electrode was placed in stratum oriens (Fig. 2A). The input-output response of PV INs with BACE1 deletion (BACE1;Ai9;PV-Cre) to stimulation of increasing intensity was not changed compared to control PV INs (Ai9;PV-Cre) (Fig. 2B, C, D). Additionally, BACE1 deletion did not alter the paired-pulse ratios (PPRs) of AMPAR EPSCs, an indicator that inversely correlates with presynaptic release probability [26] at any given inter-stimulus intervals (Fig. 2E). Similarly, the rectification index calculated from ratios of AMPAR EPSCs holding at + 40 mV to that at -60 mV (Fig. 2F, G), and either rise or decay kinetics of AMPAR EPSC (Fig. 2H, I) were not influenced by BACE1 deletion in PV INs. These data suggest that conditional BACE1 knockout would not change channel properties and basic synaptic transmission of AMPARs on CA1 PV INs from adjacent PNs in the microcircuit. As glutamatergic synaptic transmission also requires NMDAR responses, we measured the evoked NMDAR EPSCs in CA1 PV INs at + 40 mV

potential. Intriguingly, a significant increase in response to higher stimulus intensities (Fig. 2J, K, L, 15–20 V) was discovered in PV INs with BACE1 deletion compared to control neurons. The enhanced NMDAR EPSCs may result from postsynaptic components since the presynaptic release probability revealed by PPRs of AMPAR EPSCs was not changed by BACE1 deletion in the PV INs. Furthermore, we did not find any changes in the current-voltage (I-V) relationship (Fig. 2M, N) in the PV INs. It suggests an intact conductance of NMDARs in the neurons with BACE1 deletion.

BACE1 deletion made more NMDARs recruited in the postsynaptic membrane but left intact the reliability in synaptic integration of CA1 PV INs.

Our next question is whether BACE1 deletion can make more NMDARs recruited in the postsynaptic membrane of CA1 PV INs in the local microcircuit. The activity-dependent number of NMDARs can be read out by MK-801 treatment in a use-dependent manner [27], which is characterized by a greater degree of blockade with greater activation of receptors by agonist [28–30]. The neuronal excitability is not only determined by the intrinsic electrical properties but also influenced by synaptic transmission in a network. As a coincidence detector, NMDAR contributes to the excitability of neurons [31]. Therefore, we applied presynaptic paired-pulse (50 ms interval) stimulation at 0.1 Hz in stratum oriens and recorded the firing of CA1 PV INs in response to 500ms-long threshold-crossing step-currents before and after the stimulus. The stimulation was accompanied by rapid MK-801 washing-in (Fig. 3A). The control PV INs displayed an unremarkable change in the discharge frequency at 20 min after MK-801 treatment (Fig. 3B, left column, Fig. 3C, D). Intriguingly, the PV INs with BACE1 deletion showed a rapid response as short as 5 min to the same treatment, with a significant decrease at 20 min (Fig. 3B, right column, Fig. 3E, F). The result suggested that the BACE1 deletion made much more postsynaptic NMDARs recruited.

We asked whether the extra recruited NMDARs on postsynaptic portions disturb the information integration of PV INs in the hippocampal network. We examined spikes of PV INs to repetitive activation of presynaptic fibers in stratum oriens with current-clamp configuration. Unexpectedly, spikes were reliably produced during 20 stimuli of the excitatory synapses at frequencies of 5, 40, 100, and 200 Hz, respectively, in both Ai9;PV-Cre neurons and $BACE1^{fl/fl}$;Ai9;PV-Cre neurons (Fig. 3G-K). It indicates that PV INs remained the functions to reliably integrate information at a broad frequency spectrum of hippocampal oscillatory activity [32–35] though BACE1 was deleted from the cells.

Reorganized inhibitory/excitatory synaptic transmission on CA1 PNs by BACE1 deletion in PV INs in a non-uniform pattern

The next question is how the phenotypes of the PV INs may contribute to the CA1 microcircuit. We identified CA1 superficial and deep layer PNs based on their location and morphology [36, 37] and performed whole-cell recordings (Fig. 4A). We confirmed that BACE1 deletion in PV INs did not change the dendrite spine density of CA1 PNs by labeling the recorded neurons with biocytin in the pipette solution (Fig. 4B). We recorded the spontaneous IPSCs of CA1 deep layer PNs, preferentially innervated by the basket PV INs in the CA1 local circuit [37]. The PNs in $BACE1^{fl/fl}$;PV-Cre mice showed an increased

frequency (Fig. 4C, E) while an unaltered amplitude (Fig. 4C, D) of sIPSC compared to control neurons ($BACE1^{fl/fl}$). It suggests that the spontaneous inhibitory inputs to the deep layer PNs were exaggerated by BACE1 conditional knockout. The reversal potential of EPSC was supposed to be at 0 mV in our recording system. Therefore, the evoked excitatory (holding at -60 mV) and inhibitory synaptic currents (holding at 0 mV) were recorded in the same PN without synaptic blockers. A theta glass electrode was placed in Schaffer collateral (SC) to stimulate PNs to figure out whether the homeostasis of the CA1 network was affected (Fig. 4A). Furthermore, to distinguish changes in different sublayer PNs, we recorded superficial layer PNs and deep layer PNs separately in each slice under incremental stimulation of SC. Intriguingly, we found a distinct pattern in these two subpopulations of $BACE1^{fl/fl}$;PV-Cre mice compared to their $BACE1^{fl/fl}$ littermates. Note intact IPSC while decreased EPSC in deep layer PNs (Fig. 4F, H, I), whereas a decreased IPSC and an unaltered EPSC in superficial layer PNs (Fig. 4G, L, M). Similarly, the ratio of IPSC to EPSC (IPSC/EPSC) in $BACE1^{fl/fl}$;PV-Cre PNs was increased in the deep layer while decreased in the superficial layer under the maximal SC stimulation (Fig. 4J, N). The results indicate that, on the one hand, BACE1 deletion in PV INs impaired the inhibitory/excitatory transmission (I/E) balance in CA1 PNs; on the other hand, the I/E imbalance was not uniform in the CA1 pyramidale. We analyzed the Pearson correlation coefficients in these two subpopulations to know the relevance between the IPSC and the EPSC on the same CA1 PN. As shown in Fig. 4K, O, for either deep layer PNs (r = 0.6394, $^{**}p = 0.0077$) or superficial layer PNs (r = 0.5381, $^{*}p = 0.0175$) in $BACE1^{fl/fl}$ mice, there was a significant correlation between IPSC and EPSC. In $BACE1^{fl/fl}$;PV-Cre mouse CA1, PNs in the deep layer exhibited a pronounced correlation (r = 0.8836, $^{****}p < 0.0001$) between IPSC and EPSC compared to that of $BACE1^{fl/fl}$ mice. Contrary to the deep layer, PNs in the superficial layer of $BACE1^{fl/fl}$;PV-Cre CA1 displayed an uncorrelation between IPSC and EPSC (r = 0.2551, $p = 0.3403$), which deviated far from $BACE1^{fl/fl}$ mice. The results led us to hypothesize that the superficial layer PN was the most immediately affected principle cell by the disruption of CA1 microcircuit mediated by basket PV INs with BACE1 deletion.

Consistent with the evoked EPSC result (Fig. 4H, L), in $BACE1^{fl/fl}$;PV-Cre mouse CA1, the amplitude of AMPAR EPSCs of deep PNs was significantly attenuated under 50–100 μA stimulus intensity compared to the control neurons in $BACE1^{fl/fl}$ mouse (Fig. 4P). The input-output slope of AMPAR EPSCs in CA1 deep PNs was also decreased by BACE1 deletion in PV INs (Fig. 4Q). Whereas the PPRs of AMPAR EPSCs at multiple inter-stimulus intervals (Fig. 4R) were not affected by BACE1 deletion, suggesting that the suppressed AMPAR EPSCs were not due to the presynaptic release probability. Notably, the CA1 superficial PNs displayed an enhanced AMPAR EPSC responding to the maximal stimulus intensity (20 V with a theta glass electrode, Fig. 4S). Nevertheless, the input/output slope and the PPRs were unchanged (Fig. 4T, U). It implied that the impairment of AMPAR EPSCs of CA1 PNs in the CA3-SC-CA1 long circuit has a heterogeneous pattern. It was consistent with the non-uniform reorganization of inhibitory/excitatory synaptic transmission on the CA1 PNs and may probably contribute to distinct functions of long-distance targets of CA1 PNs [38]. Note that the alteration of AMPAR EPSCs still existed in the conditional knockout mice at six months old (Supplementary Fig. 6), indicating that the phenotype is not random in the neurodevelopment.

According to a reported working model [38]: in the CA1 network, basket PV INs provide larger perisomatic inhibitory synaptic inputs to the deep CA1 PNs than the superficial CA1 PNs. Meanwhile, PV INs receive more significant excitatory inputs from the superficial CA1 PNs than the deep ones. In addition, SC excitation from CA3 is more robust in the superficial PNs. Thus, the microcircuit organization between the heterogeneous CA1 PNs and the adjacent PV INs established a preferential recurrent inhibitory motif from the superficial to the deep layer. However, the BACE1 deletion in CA1 PV INs disrupted the recurrent inhibitory network with an escape of superficial PNs from the microcircuit motif. In this abnormal network (Fig. 4V), the excitatory outputs of deep CA1 PNs appeared to be eventually impaired since their evoked EPSC was significantly reduced (Fig. 4H).

Specific local recovery of BACE1 expression restored the synaptic transmission in an enzymatic-dependent manner.

Further, we sought to confirm if BACE1 deletion in PV INs played a causative role in the increment of NMDARs response in PV INs and the final suppression of AMPAR EPSCs in CA1 PNs. In addition, whether the b-secretase enzymatic activity-dependent mechanism was involved in these phenotypes is a critical relevant question, given that BACE1 is an aspartyl protease [10]. Therefore, we constructed vectors of recombinant adeno-associated virus (rAAV) with a double inverse open reading frame (DIO), in which wild-type *Bace1* gene (BACE1^{WT}) or B*ace1* gene with D93A mutant (BACE1^{D93A}) were inserted. The D93A mutant was designed to disrupt the enzyme active site of BACE1 as an aspartyl protease, whereas it did not influence its maturation [39]. The eGFP gene was used as a non-fused reporter separated by P2A to indicate the target gene expression. The expression vector of rAAV-DIO-eGFP or rAAV-DIO-BACE1^{WT}-P2A-eGFP or rAAV-DIO-BACE1^{D93A}-P2A-eGFP was stereotactically injected into hippocampal CA1 of BACE1$^{fl/fl}$;PV-Cre mouse at the age of 2-months. After three weeks, these mice were subjected to slice preparation and whole-cell recording (Fig. 5A). The expression of the infected target proteins was double-checked by co-expressed eGFP signal, and the immunofluorescent staining with anti-parvalbumin and anti-BACE1 antibodies (Fig. 5B). The extracellular electrode stimulation at 20 V stimulus intensity in CA1 SO (Fig. 5C) evoked a fallback of NMDAR EPSCs in PV INs of BACE1$^{fl/fl}$;PV-Cre mice injected with rAAV-DIO-BACE1^{WT}-P2A-eGFP compared to BACE1$^{fl/fl}$;PV-Cre mice injected with rAAV-DIO-eGFP. While the BACE1$^{fl/fl}$;PV-Cre mice injected with rAAV-DIO-BACE1^{D93A}-P2A-eGFP displayed a comparable NMDARs response to the control mice infected with rAAV-DIO-eGFP (Fig. 5D, E, F). The result indicates that the BACE1 expression was necessary and sufficient for the homeostasis of the postsynaptic NMDAR response in CA1 PV INs. Moreover, the enzymatic activity of BACE1 contributed to most, if not all, of the effect.

As expected, upon the stimulation of SC (Fig. 5G), the AMPAR EPSCs in CA1 deep layer PNs of BACE1$^{fl/fl}$;PV-Cre mice injected with rAAV-DIO-BACE1^{WT}-P2A-eGFP recovered to an average normal level compared to eGFP expressed control mice (Fig. 5H, I). Consistently, expression of BACE1^{D93A}-eGFP in CA1 PV INs with BACE1 deletion failed in rescuing AMPAR EPSCs in the PNs, implying the enzymatic activity of BACE1 determined the restoration of AMPAR EPSCs to the long projection inputs.

In addition, because we expressed the target proteins only in adult CA1, these findings ruled out: 1. the phenotypes in the BACE1 conditional knockout mouse were from disorders of embryonic development; 2. the abnormal CA1 motif resulted from dysfunction of local PV INs, rather than from disruption of long projecting PV neurons located in other brain nuclei, e.g., medial septum [33, 40, 41].

BACE1 deletion in PV INs resets the priming of fear memory extinction.

To further explore whether BACE1 in CA1 PV INs contributes to hippocampal-dependent learning and memory processing, we applied the paradigm of contextual fear conditioning (CFC) in the mice. Consistent with the finding of unaltered evoked spikes of PV INs with BACE1 deletion (Fig. 3G-K), the difference between BACE1$^{fl/fl}$ and BACE1$^{fl/fl}$;PV-Cre mice did not occur in the encoding and the extinction of conditioned fear memory (Supplementary Fig. 7).

Next, we want to know if there is a behavioral phenotype that CA1 PV INs could explicitly cause with BACE1 deletion. We expressed hM4Di, an inhibitor designer receptor exclusively activated by a designer drug (DREADD) in CA1 PV INs by stereotaxic injection of Cre-dependent adeno-associated virus (AAV-EF1a-DIO-hM4Di-GFP). The AAV-EF1a-DIO-GFP was injected as a control in PV-Cre;Ai9 or BACE1$^{fl/fl}$;PV-Cre mouse CA1 region (Fig. 6A). Two weeks later, we prepared acute slices and identified the infected PV INs by fluorescent protein (GFP) (Fig. 6B, the left). The whole-cell recording was performed to verify the inhibitory effect of the DREADD system on the PV INs (Fig. 6B, the right). Whereas hM4Di-GFP expressing neuron showed an obvious hyperpolarized response (from ~-60mV to ~-67mV), GFP expressing control neuron displayed a steady membrane potential (~-60mV) to hM4Di agonist clozapine-N-oxide (CNO) (3 μM) treatment in perfusion. Most importantly, the hM4Di inhibition was reversible within a window of 20 min (Fig. 6B). It could help elucidate a possible effect of the CA1 microcircuit in any given stage of memory processing more accurately.

Three weeks after the virus injection, animals were intraperitoneally injected with CNO twice daily during the CFC procedure (Fig. 6C). The PV-Cre;Ai9 and BACE1$^{fl/fl}$;PV-Cre mice with or without hM4Di expressing displayed a comparable performance in the tasks of contextual fear conditioning and cued test (Fig. 6D). It indicates that the CA1 PV INs had no contribution to the contextual fear memory acquisition, and BACE1 deletion did not change the phenotype. All subjected mice displayed a low freezing level in the new context, suggesting the freezing behavior was mainly attributed to recognizing the context associated with an aversive foot shock (Fig. 6C). As expected, the mice showed a virtually similar freezing behavior in three rounds of fear conditioning (Fig. 6E), indicating an average ability to learn to associate a context with an aversive footshock. Intriguingly, the contextual fear extinction test revealed with DREADD inhibition a pronounced difference between PV-Cre;Ai9 mice and BACE1$^{fl/fl}$;PV-Cre mice, although there was no change between these two groups of mice without DREADD inhibition (Fig. 6F, the left). After DREADD inhibition of the CA1 PV INs, the PV-Cre;Ai9 mice exhibited a trend of slow extinction (Fig. 6F, the middle), while the BACE1$^{fl/fl}$;PV-Cre mice showed a faster extinction (Fig. 6F, the right). The unexpected results led us to propose that the BACE1 in CA1 PV INs probably played a crucial role in the priming of fear memory extinction.

Discussion

BACE1 has shown effects on synaptic transmission and plasticity [7, 9, 15, 16, 42–44], while the circuit mechanism needs to be clarified. We used a cell-type-specific knockout approach to elucidate a plausible working model. BACE1 in PV INs regulating the local circuit of hippocampal CA1 (Supplementary Fig. 8): the microcircuit organization between the heterogeneous CA1 PNs and the adjacent PV INs established a preferential recurrent inhibitory motif from the superficial to the deep layer [38]. We found that conditional BACE1 deficiency in dependence on its enzymatic activity exaggerated the NMDAR-mediated synaptic transmission onto PV INs in the CA1 microcircuit. It led to an escape of superficial PNs from the CA1 network motif, in which the excitatory outputs of deep CA1 PNs appeared to be eventually impaired, presumably because of these changes in the CA1 network, resetting the priming of conditioned fear memory extinction. Given that BACE1 inhibition displayed side effects or cognitive worsening concerning a prime drug target for treating AD [8, 10], it is reasonable to suggest that the combination of BACE1 and NMDAR targeting may be a potential path in AD treatment.

In the hippocampal CA1, the PV INs constitute 24% of all GABAergic neurons, which form 11% of the total neuronal population in the region [35]. The fast-spiking PV-positive neurons among all types of PV INs in CA1 have been well studied and displayed an ability to assemble their targeting PNs to form a uniform network motif, which contributes to the hippocampal network oscillations adapted to cognitive tasks [33, 35, 38, 45]. Here we have virtually chosen PV INs following the three sets of criteria [35]: 1) PV-expressing; 2) morphological properties and its location nearby the stratum pyramidale; 3) most importantly, the fast-spiking pattern of the action potential (Fig. 1G). In addition, PV INs with BACE1 deletion in our conditional knockout mouse were located mainly at stratum pyramidale and among PNs (Fig. 1D, Supplementary Fig. 3), indicating the salient impact of BACE1 in regulating the hippocampal network. Intriguingly, we noticed a different pattern of BACE1 expression between late-born and early-born PV neurons [23] in CA1 (Fig. 1D), implying, on the one hand, the time-spectrum of *Bace1* transcription, on the other hand, a possible distinct role of BACE1 in these two types of PV neurons. This argument about the interaction of BACE1 expression and PV neuronal development deserves further study.

Previous studies suggested that auxiliary β-subunits of the voltage-gated sodium channels and KCNE1/KCNE2 auxiliary subunits of the voltage-gated potassium channels were substrates of BACE1 enzymatic cleavage [18, 46–48]. Moreover, the voltage-gated sodium and potassium channels interact with BACE1 independent of its enzymatic activity [21, 49–51]. In our study, the unchanged fast-firing frequency and rheobase of PV INs with BACE1 deletion (Fig. 1) ruled at least partially out a possible role of the voltage-gated sodium channel and the Kv3 subunits in the regulation of the circuit motif involving BACE1, considering the Kv3 is highly expressed in the CA1 PV INs [35, 52]. In addition, the intact evoked spikes in PV INs (Fig. 1, Fig. 3) denied the contribution of M-current, which is regulated by BACE1, to modulating the subthreshold integration of synaptic inputs [49].

Notably, there were inconsistent findings on Nav subunits expression in BACE1-null mice [17, 18] that may be attributed to a complicated neuronal response in extremely intricate networks due to the systemic

BACE1 knockout. By MK-801 treatment, we can identify the salient role of the synaptic NMDARs in the effect of BACE1 on the efficiency of neuronal discharge based on the coincidence detective function of NMDARs (Fig. 3). However, the mechanism by which BACE1 deletion increases the NMDAR EPSCs in PV INs is thought-provoking (Fig. 2). It is supposed to be related to the aspartic protease activity of BACE1 since the expression of D93A mutant BACE1 did not restore the NMDAR EPSCs, while the wild-type BACE1 did (Fig. 5). Several synaptic cell-adhesive molecules, e.g., neuroligins, are found as the substrates of BACE1 sheddase [53]. Within the neuroligin family, neuroligin-1, as a postsynaptic cell-adhesion molecule of excitatory synapses [54], can interact with the NMDAR subunit, GluN1 to recruit NMDARs [55] and mediate the basic synaptic transmission [56]. Moreover, synaptic NMDAR activation can trigger acute proteolytic cleavage of neuroligin-1, and as a feedback regulation, neuroligin-1 cleavage depresses synaptic transmission [57, 58]. Combining these findings, we propose that BACE1 deletion might disrupt the activity-dependent proteolytic processing of neuroligin-1, which recruits much more NMDARs to the excitatory synapse.

We discovered a dominant effect of BACE1 in PV INs on the homeostasis of the CA1 microcircuit, which is critical for information integration during learning and memory [23, 35, 38, 59, 60]. In learning and memory, the hippocampus integrates inputs from associative brain regions. It sends outputs to cortical areas, including the medial prefrontal cortex (mPFC), entorhinal cortex, and amygdala, through long-distance projecting PNs [38, 61, 62]. The projecting PNs within CA1 are segmentally organized into local circuits with fast-spiking PV INs to form non-uniform inhibitory-excitatory connectivity motifs [37]. The featured local circuit interaction benefits the computation of parallel tasks [38, 62]. While the normal activation of CA1 PV INs accelerates the contextual fear extinction [59], that is consistent with our observation in PV-Cre mice with chemical genetic manipulation (Fig. 6F). Notably, the cell-type-specific knockout approach was not remarkable enough to directly induce deficits in memory encoding, consolidation, and extinction in the orthodox behavior paradigm (Fig. 6 and Supplementary Fig. 7). Interestingly, we discovered here that the BACE1 deletion virtually changed the priming state of the CA1 microcircuit for contextual fear extinction (Fig. 6). In addition, we did not observe morphological changes in dendritic spines of CA1 PNs (Fig. 4B) in our conditional knockout mice, in markable contrast to the systemic BACE1 knockout mice [9], excluding the impact of the cell-type-specific BACE1 deficiency on the structural development and excitatory synaptogenesis of the hippocampal network.

The critical point is that the NMDAR response was abnormally enhanced by BACE1 deletion in PV INs (Fig. 2, Fig. 3), leading us to propose a combined treatment strategy for AD. Recently, the positive allosteric modulation of the metabotropic glutamate receptor 1 (mGluR1) has been suggested to counteract the BACE1 deletion- or inhibition-mediated deficits in synaptic vesicle release [44]. These findings suggest a new path to treat AD with BACE1-targeting and synaptic receptors-modulating.

Limitation

we do not yet know the mechanism of the pyramidal non-cell-autonomous response of AMPAR in CA1 to dysfunction of local microcircuit due to impairment of PV INs. Synaptic adhesion molecules, such as

Neurexins/Neuroligins, are implicated in rescaling excitatory and inhibitory synapses [63] might be a reasonable explanation. However, it needed to be verified by explicit experiments.

Materials And Methods

Animals

The BACE1$^{fl/fl}$ homozygotes were first bred and crossed with PV-Cre mice (JAX stock #008069) to obtain BACE1$^{fl/+}$;PV-Cre mice, female of which were crossed with male BACE1$^{fl/fl}$ mice to get BACE1$^{fl/fl}$;PV-Cre mice. In addition, to obtain mice carrying Ai9-labeled PV neurons, we first crossed male BACE1$^{fl/fl}$ mice with female Ai9;PV-Cre (JAX stock #007905) homozygotes and got BACE1$^{fl/+}$;Ai9;PV-Cre mice, which were then hybridized with BACE1$^{fl/fl}$ mice, and finally, BACE1$^{fl/fl}$;Ai9;PV-Cre strain was achieved. The strains of BACE1$^{fl/fl}$, BACE1$^{fl/fl}$;PV-Cre, BACE1$^{fl/fl}$;Ai9;PV-Cre were maintained by crossing BACE1$^{fl/fl}$ with either BACE1$^{fl/fl}$;PV-Cre or BACE1$^{fl/fl}$;Ai9;PV-Cre mice, and subjected to experiments. The PV-Cre;Ai9 heterozygotes were bred as control mice. All these animals were maintained on the background of C57BL/6J. Female and male mice were used unbiasedly in this study.

Conditional knockout mouse

The *loxP*-flanked (flox) targeting vector was designed and constructed using the recombineering techniques described in the *Supplementary methods and Supplementary Figure 1*. The endogenous *bace1* promoter drives the expression of the inserted gene. The construct was electroporated into C57BL/6 mouse embryonic stem (ES) cells. The ES clones carrying the targeting vector were screened by G418 resistance and were double confirmed by PCR using primers outside the construct paired with primers inside the neo cassette, and Southern blot using 3'-Probe, 5'-Probe, and Neo probe. After analysis of karyotype, correctly targeted ES cells were injected into recipient blastocysts. The resulting chimeric animals were crossed to C57BL/6 mice. The neomycin resistance cassette was removed by breeding mice expressing FLP recombinase, and the *Flp* transgene was finally bred out. The F1 heterozygotes were intercrossed to produce homozygotes. All mice were with c57BL background. The primers recognizing fragments either containing the first *loxP* site or not were used in genotyping as follows:

forward primer: 5'-GGCAGAGGTTGGACCTGACTAG-3';

reverse primer: 5'-ATTGTCCTCTAACCTCCATACACAAG-3'

Stereotaxic injection of virus

After anesthetized with 1.2% avertin (240 mg/kg body weight) by intraperitoneal injection, mice were fixed in a stereotaxic apparatus and injected with an AAV virus containing specific gene sequences into the bilateral brain. The viruses were custom-made and provided by Obio Technology Co. Ltd. (China). The site of stereotaxic injection was: 2.0 mm posterior to the bregma; 1.0 mm lateral to the midline; 1.2 mm below the brain surface for the injection of the CA1 region. Viral solution (200 nL/site) was injected using a

microinjector coupled with a glass micropipette at a rate of 75 nL/min. The micropipette was held in the target place for an additional 10 min at the end of the injection, and carprofen (5 mg/kg body weight) was injected after surgery to relieve the pain.

Electrophysiological recordings

Acute brain slices preparation

A mouse was quickly transcardially perfused by an ice-cold, high-sucrose cutting solution containing (in mM): 10 D-glucose, 213 sucrose, 1 NaH_2PO_4, 26 $NaHCO_3$, 3 KCl, 0.5 $CaCl_2$, 5 $MgCl_2$ at a rate of 10 ml/min after anesthetized by intraperitoneal injection of 10% chloral hydrate (300 mg/kg). After that, the mouse brain was quickly removed and fixed by 502 glue on a cutting box of Leica vibratome (Leica, VT1200S), and 300 μm coronal slices were cut (rate: 0.2 mm/s; the amplitude of vibration: 0.8 mm) in the ice-cold high sucrose cutting solution. The dorsal hippocampus slices were obtained, and the cutting process was limited to 5 min. The slices were immediately transferred to and bubbled in an incubation chamber filled with artificial cerebrospinal fluid (ACSF) containing (in mM): 11 glucose, 119 NaCl, 1 NaH_2PO_4, 26 $NaHCO_3$, 2.5 KCl, 2.5 $CaCl_2$, 1.3 $MgSO_4$, pH=7.4, at 32^oC for 30 min, and then left at room temperature (25^oC) for a further 1 h before recording. During recordings, the slices were placed in a recording chamber constantly perfused with the same ACSF. All liquid was gassed continuously in a mixture of 95% CO_2 and 5% O_2. The perfusion speed was maintained at 2 ml/min, except where noted. The HEKA EPC10 patch-clamp signal acquisition system was used for data acquisition, sampling at 20 kHz for current-clamp and 10 kHz for voltage-clamp recording. Fitmaster (HEKA) and pClamp10.4 (Axon Instruments) or Mini analysis software (Version 6.0.7) were used for data analysis.

Electrophysiological recordings

PV INs were identified by the presence of Tdtomato under fluorescence microscopy (Olympus BX51WI, Olympus Optical) and visualized by infrared differential interference. PNs and PV INs in CA1 were recorded in whole-cell mode. Borosilicate glass (Sutter Instrument) electrodes with resistance of 3–5 MΩ were pulled and filled with intracellular solution containing (in mM): 6 KCl, 124 K-gluconate, 1 $MgCl_2$, 5 EGTA, 10 HEPES, 0.5 $CaCl_2$, 0.5 Na_2GTP, 5 MgATP, 12 Phosphocreatine (pH=7.25, OSM=290) for current-clamp recording; 65 KCl, 65 K-gluconate, 1 $MgCl_2$, 5 EGTA, 10 HEPES, 0.5 $CaCl_2$, 0.5 Na_2GTP, 5 MgATP, 12 Phosphocreatine (pH=7.25, OSM=290). The whole-cell recordings were performed as described previously [64]. In brief, resting membrane potential was immediately recorded once the acquisition of the whole-cell configuration. The membrane input resistance and evoked excitability of neurons were measured by 500 ms step-current injections from -30 pA to +200 pA with a step of 10 pA in current-clamp mode. The neuron's rheobase was determined by a series of 3 ms step-current injections with a step of 10 pA until the action potential was evoked. In voltage-clamp configuration, the series resistance (Rs) was measured and monitored during the whole process of recordings, and neurons whose Rs were above 30 MΩ were excluded from the analysis. Rs and membrane capacitance (Cm) are monitored [64] by applying a hyperpolarization pulse (-5 mV) at the beginning and the end of each recording sweep. Neurons that

displayed unstable resting membrane potential in current-clamp mode or aberrant spiking patterns were excluded from the analysis.

In voltage-clamp recording, Evoked EPSC and IPSC/EPSC ratio of neurons were recorded with intracellular solution containing (in mM): 135 Cs-methanesulphonate, 0.5 EGTA, 10 HEPES, 8 NaCl, 0.5 Na_2GTP, 5 MgATP, 12 Phosphocreatine, 20 Leupeptin, 2 QX-314, 0.1 spermine (pH=7.25 OSM=290). During the physiological experiment: 50 μM PTX and 50 μM APV were added to the ACSF for AMPAR-EPSC achievement; 50 μM PTX and 25 μM CNQX for NMDAR-EPSC recording, and no blocker for IPSC/EPSC ratio acquisition. When recording evoked EPSC of PV neurons, the stimulating metal electrode (CBBEB75, Frederick Haer) or glass theta electrode was placed in CA1 oriens alveus layer five cell bodies away from the recording neuron. When recording evoked EPSC and IPSC/EPSC ratio of pyramidal neurons, a stimulating electrode was placed in the Schaffer collateral at CA1 100 μm away from the recording neuron. Cells were held at −60 mV for recording AMPAR EPSCs, or at +40 mV for NMDAR EPSCs, while single stimulating afferent inputs (A-M System 2100) ranged from 0 μA to 100 μA (10 μA as a step) with metal electrode or from 2.5 V to 20 V (2.5 V as a step) with glass theta electrode. The IPSC/EPSC ratio was calculated as the ratio of evoked IPSCs at 0 mV to evoked EPSCs at −60mV while single stimulating afferent inputs were described above. The I–V relationship of AMPAR EPSCs or NMDAR EPSCs was measured at holding potentials from −60 mV to +40 mV with a step of 10 mV in voltage-clamp mode with 100 μA stimulation. Under recording AMPAR EPSCs, the single stimulating afferent inputs were changed into pairs of stimulation. The inter-stimulus interval was set at 20 ms, 50 ms, 100 ms, and 200 ms, respectively. Paired AMPAR EPSCs (P1, P2) were recorded, and the paired-pulse ratio was calculated as the ratio of P2/P1. A single exponential equation calculates the decay time Constance (τ) of AMPAR-EPSC: $I(t)= I *e^{-t/\tau}$.

Drug treatment and spikes evoking

We immediately switched to current-clamp mode upon whole-cell break-in and recorded resting membrane potential (RP). Recording membrane potential in the presence of PTX (50 mM) and CNQX (25 mM) for at least 10 min to allow equilibrium of pipette solution with the intracellular fluid and make the blockers work at total capacity. MK-801 (20 mM) was added to ACSF perfusion, in which the perfusion speed was set at 5 ml/min to ensure a sustained use-dependent blockade of the NMDAR channel [27]. The minimal necessary stimulation intensity to evoke spiking of PV IN in current-clamp mode with a glass theta electrode was determined by two consecutive stimulations (paired-pulse) at a 50 ms interstimulus interval (Supplementary Figure 2). The same stimulation intensity, in the same way, was utilized at a frequency of 0.1 Hz in the MK-801 treatment. After 5 min stimulation, an additional process of membrane potential was recorded for 10 min in the presence of MK-801, PTX, and CNQX, followed by a 5 min recording in which all blockers were washed out. Three series of action potentials induced by 500 ms step-current injections were obtained at time-point: 1) before MK-801 was applied, 2) after presynaptic stimulation, and 3) at the end of the recording process, respectively. The membrane potential was monitored throughout the whole process of recording. Those cells with abnormal potential that could not generate action potential upon stimulation of step-current injections were excluded. PV IN was identified,

clamped, and recorded for CNO treatment in the current-clamp configuration. The membrane potential was continually monitored during the perfusion of ACSF containing clozapine-N-oxide (CNO) at the final concentration of 3 mM.

Contextual fear conditioning and extinction

Two weeks after the injection of the AAV virus (AAV2/9-EF1a-DIO-hM4D(Gi)-GFP or AAV2/9-EF1a-DIO-GFP) in the hippocampal CA1 region (AP: -2.0 mm, ML: 1.0 mm, DV: 1.2 mm, 300 nL/site), 2.5-month-old mice were used for the experiment. During all 5 d of the behavioral procedure, mice were treated twice one day with 10 mg/kg clozapine-N-oxide (CNO) intraperitoneally injected 1 h before and 12 h after the behavior experiment. On day 1, the mice were allowed to habituate to the testing room for 1 h. During training, the mice were allowed to stay in the training cage (grid floor, opaque triangular ceiling, and 5% acetic acid) for 3 min to recognize the context, followed by 3 rounds of CS-US (conditioned stimulus-unconditioned stimulus) training. For each round of training, 2 s foot shock (0.6 mA) was given at the end of 30 s continuous tone (4000 Hz, 80 dB). The cage was cleaned with 10% alcohol after each test. On day 2, the mice were exposed to the training cage again for 3 min to confirm the acquisition and consolidation of the hippocampal-dependent contextual fear memory by reading out the freezing performance. The automatically captured freezing behavior was used to evaluate the fear level. After 2 h, the mice were placed in a new neutral cage (with a smooth board, without a triangular ceiling and acetic acid). The mice were allowed to explore for 3 min, during which the freezing behavior was recorded. After that, the mice were exposed to the same sound stimulation as in the training round for 3 min. The freezing level was measured to assess hippocampal-independent behavior in the cued test. From day 3 to day 5, the mice were subjected to an extinction test. The mice were placed in the training cage for 3 min twice a day, with an interval of 2 h between the two trials. The freezing time was recorded and analyzed with a video freeze® software system (Med Associates Inc.).

Biocytin labeling and immunostaining

During whole-cell recording, the neuronal spine morphology of CA1 neurons was labeled by adding biocytin (0.04%) to the pipette solution. After recording, slices were fixed overnight in paraformaldehyde (4%), followed by permeation of 0.5% Triton X-100 for 20 min and incubation with streptavidin-coupled Alexa 488 (Invitrogen) for 2 hr at RT. The spine density was determined by 3D morphological imaging captured in stacks of 100 μm at Z step of 0.5 μm by a 60 X oil objective lens (Olympus, FV3000) and reconstructed using Imaris filament tracer (Bitplane). During morphometric analyses, the observer was blinded to the mouse genotype.

The mouse brain was removed sequentially after anesthesia and transcardial perfusion with saline and paraformaldehyde (4%). The 30 μm thick brain sections were cut with a vibratome (Leica VT1000S) in phosphate-buffered saline (PBS). After being permeated with 0.3% Triton X-100 for 30 min and blocked with 10% goat serum for 30 min, slices were incubated with primary antibodies (BACE1, Abcam, ab108394, 1:500; parvalbumin, Sigma, P3088, 1:500) at 4^{o}C overnight, followed by incubation with Alexa

Fluor-488, -594 or -647 (Invitrogen, A11008, A11037, A21244, 1:500,). Slices were covered with microscope cover glasses. Paired sections from the control and experimental brains were attached to a slide, and three pairs of brains were used for confocal imaging. After staining, all sections were imaged under the same capture parameters with Confocal Laser Scanning Microscope (Olympus FV3000).

Statistical analysis

All data were first tested for Normality. Data sets that passed the normality test were subjected to parametric tests with unpaired t test for two groups comparison or one/two-way ANOVA for more than two groups comparison. Nonparametric tests analyzed the data which did not pass the normality test. The analysis software was GraphPad Prism 8.0.1. The description of statistical analysis in detail is available in the *Supplementary information.*

Declarations

Acknowledgment

We thank Hua Li and Hua Wei from Capital Medical University, China for their technical support. This work was supported by the National Natural Science Foundation of China (81771145, 81971004, 81571038 to YZ), Beijing Natural Science Foundation (5202006 to YZ).

Authors' contribution:

virus-injection, tests of behavior and chemogenetics were performed by Xuansheng Xiao; physiological data were provided by Xiaotong Wang, Ke Zhu and Yan Zheng; Lijuan Li performed immunostaining and reconstruction of dendritic spine; Xuansheng Xiao and other co-authors performed quality control and statistical analysis in double-blind for data. Yan Zheng designed the study and wrote the manuscript with all other authors' help.

Conflict of interest

The authors declare no competing interests.

Supplementary information is available at MP's website.

References

1. Hussain I, Powell D, Howlett DR, Tew DG, Meek TD, Chapman C, et al. Identification of a novel aspartic protease (Asp 2) as beta-secretase. Mol Cell Neurosci. 1999;14:419-27.
2. Lin X, Koelsch G, Wu S, Downs D, Dashti A Tang J. Human aspartic protease memapsin 2 cleaves the beta-secretase site of beta-amyloid precursor protein. Proc Natl Acad Sci U S A. 2000;97:1456-60.
3. Sinha S, Anderson JP, Barbour R, Basi GS, Caccavello R, Davis D, et al. Purification and cloning of amyloid precursor protein beta-secretase from human brain. Nature. 1999;402:537-40.

4. Vassar R, Bennett BD, Babu-Khan S, Kahn S, Mendiaz EA, Denis P, et al. Beta-secretase cleavage of Alzheimer's amyloid precursor protein by the transmembrane aspartic protease BACE. Science. 1999;286:735-41.
5. Yan R, Bienkowski MJ, Shuck ME, Miao H, Tory MC, Pauley AM, et al. Membrane-anchored aspartyl protease with Alzheimer's disease beta-secretase activity. Nature. 1999;402:533-7.
6. Yan R, Fan Q, Zhou J Vassar R. Inhibiting BACE1 to reverse synaptic dysfunctions in Alzheimer's disease. Neurosci Biobehav Rev. 2016;65:326-40.
7. Das B Yan R. Role of BACE1 in Alzheimer's synaptic function. Transl Neurodegener. 2017;6:23.
8. Wessels AM, Lines C, Stern RA, Kost J, Voss T, Mozley LH, et al. Cognitive outcomes in trials of two BACE inhibitors in Alzheimer's disease. Alzheimers Dement. 2020;16:1483-92.
9. Zhu K, Peters F, Filser S Herms J. Consequences of Pharmacological BACE Inhibition on Synaptic Structure and Function. Biol Psychiatry. 2018;84:478-87.
10. Hampel H, Vassar R, De Strooper B, Hardy J, Willem M, Singh N, et al. The beta-Secretase BACE1 in Alzheimer's Disease. Biol Psychiatry. 2021;89:745-56.
11. Kandalepas PC, Sadleir KR, Eimer WA, Zhao J, Nicholson DA Vassar R. The Alzheimer's beta-secretase BACE1 localizes to normal presynaptic terminals and to dystrophic presynaptic terminals surrounding amyloid plaques. Acta Neuropathol. 2013;126:329-52.
12. Cai H, Wang Y, McCarthy D, Wen H, Borchelt DR, Price DL, et al. BACE1 is the major beta-secretase for generation of Abeta peptides by neurons. Nat Neurosci. 2001;4:233-4.
13. Hu X, Hicks CW, He W, Wong P, Macklin WB, Trapp BD, et al. Bace1 modulates myelination in the central and peripheral nervous system. Nat Neurosci. 2006;9:1520-5.
14. Willem M, Garratt AN, Novak B, Citron M, Kaufmann S, Rittger A, et al. Control of peripheral nerve myelination by the beta-secretase BACE1. Science. 2006;314:664-6.
15. Laird FM, Cai H, Savonenko AV, Farah MH, He K, Melnikova T, et al. BACE1, a major determinant of selective vulnerability of the brain to amyloid-beta amyloidogenesis, is essential for cognitive, emotional, and synaptic functions. J Neurosci. 2005;25:11693-709.
16. Munro KM, Nash A, Pigoni M, Lichtenthaler SF Gunnersen JM. Functions of the Alzheimer's Disease Protease BACE1 at the Synapse in the Central Nervous System. J Mol Neurosci. 2016;60:305-15.
17. Hu X, Zhou X, He W, Yang J, Xiong W, Wong P, et al. BACE1 deficiency causes altered neuronal activity and neurodegeneration. J Neurosci. 2010;30:8819-29.
18. Hitt BD, Jaramillo TC, Chetkovich DM Vassar R. BACE1-/- mice exhibit seizure activity that does not correlate with sodium channel level or axonal localization. Mol Neurodegener. 2010;5:31.
19. Savonenko AV, Melnikova T, Laird FM, Stewart KA, Price DL Wong PC. Alteration of BACE1-dependent NRG1/ErbB4 signaling and schizophrenia-like phenotypes in BACE1-null mice. Proc Natl Acad Sci U S A. 2008;105:5585-90.
20. Cai J, Qi X, Kociok N, Skosyrski S, Emilio A, Ruan Q, et al. beta-Secretase (BACE1) inhibition causes retinal pathology by vascular dysregulation and accumulation of age pigment. EMBO Mol Med.

2012;4:980-91.

21. Lehnert S, Hartmann S, Hessler S, Adelsberger H, Huth T Alzheimer C. Ion channel regulation by beta-secretase BACE1 - enzymatic and non-enzymatic effects beyond Alzheimer's disease. Channels (Austin). 2016;10:365-78.
22. Hitt B, Riordan SM, Kukreja L, Eimer WA, Rajapaksha TW Vassar R. beta-Site amyloid precursor protein (APP)-cleaving enzyme 1 (BACE1)-deficient mice exhibit a close homolog of L1 (CHL1) loss-of-function phenotype involving axon guidance defects. J Biol Chem. 2012;287:38408-25.
23. Pelkey KA, Chittajallu R, Craig MT, Tricoire L, Wester JC McBain CJ. Hippocampal GABAergic Inhibitory Interneurons. Physiol Rev. 2017;97:1619-747.
24. Korotkova T, Fuchs EC, Ponomarenko A, von Engelhardt J Monyer H. NMDA receptor ablation on parvalbumin-positive interneurons impairs hippocampal synchrony, spatial representations, and working memory. Neuron. 2010;68:557-69.
25. Madisen L, Zwingman TA, Sunkin SM, Oh SW, Zariwala HA, Gu H, et al. A robust and high-throughput Cre reporting and characterization system for the whole mouse brain. Nat Neurosci. 2010;13:133-40.
26. Zucker RS Regehr WG. Short-term synaptic plasticity. Annu Rev Physiol. 2002;64:355-405.
27. Huettner JE Bean BP. Block of N-methyl-D-aspartate-activated current by the anticonvulsant MK-801: selective binding to open channels. Proc Natl Acad Sci U S A. 1988;85:1307-11.
28. Chen HS Lipton SA. Mechanism of memantine block of NMDA-activated channels in rat retinal ganglion cells: uncompetitive antagonism. J Physiol. 1997;499 (Pt 1):27-46.
29. Tovar KR Westbrook GL. Mobile NMDA receptors at hippocampal synapses. Neuron. 2002;34:255-64.
30. Song X, Jensen MO, Jogini V, Stein RA, Lee CH, McHaourab HS, et al. Mechanism of NMDA receptor channel block by MK-801 and memantine. Nature. 2018;556:515-9.
31. Hansen KB, Wollmuth LP, Bowie D, Furukawa H, Menniti FS, Sobolevsky AI, et al. Structure, Function, and Pharmacology of Glutamate Receptor Ion Channels. Pharmacol Rev. 2021;73:298-487.
32. Pouille F Scanziani M. Enforcement of temporal fidelity in pyramidal cells by somatic feed-forward inhibition. Science. 2001;293:1159-63.
33. Klausberger T Somogyi P. Neuronal diversity and temporal dynamics: the unity of hippocampal circuit operations. Science. 2008;321:53-7.
34. Colgin LL, Denninger T, Fyhn M, Hafting T, Bonnevie T, Jensen O, et al. Frequency of gamma oscillations routes flow of information in the hippocampus. Nature. 2009;462:353-7.
35. Hu H, Gan J Jonas P. Interneurons. Fast-spiking, parvalbumin(+) GABAergic interneurons: from cellular design to microcircuit function. Science. 2014;345:1255263.
36. Li Y, Xu J, Liu Y, Zhu J, Liu N, Zeng W, et al. A distinct entorhinal cortex to hippocampal CA1 direct circuit for olfactory associative learning. Nat Neurosci. 2017;20:559-70.
37. Lee SH, Marchionni I, Bezaire M, Varga C, Danielson N, Lovett-Barron M, et al. Parvalbumin-positive basket cells differentiate among hippocampal pyramidal cells. Neuron. 2014;82:1129-44.

38. Soltesz I Losonczy A. CA1 pyramidal cell diversity enabling parallel information processing in the hippocampus. Nat Neurosci. 2018;21:484-93.
39. Jin S, Agerman K, Kolmodin K, Gustafsson E, Dahlqvist C, Jureus A, et al. Evidence for dimeric BACE-mediated APP processing. Biochem Biophys Res Commun. 2010;393:21-7.
40. Morris NP, Harris SJ Henderson Z. Parvalbumin-immunoreactive, fast-spiking neurons in the medial septum/diagonal band complex of the rat: intracellular recordings in vitro. Neuroscience. 1999;92:589-600.
41. Wu M, Shanabrough M, Leranth C Alreja M. Cholinergic excitation of septohippocampal GABA but not cholinergic neurons: implications for learning and memory. J Neurosci. 2000;20:3900-8.
42. Filser S, Ovsepian SV, Masana M, Blazquez-Llorca L, Brandt Elvang A, Volbracht C, et al. Pharmacological inhibition of BACE1 impairs synaptic plasticity and cognitive functions. Biol Psychiatry. 2015;77:729-39.
43. Zhu K, Xiang X, Filser S, Marinkovic P, Dorostkar MM, Crux S, et al. Beta-Site Amyloid Precursor Protein Cleaving Enzyme 1 Inhibition Impairs Synaptic Plasticity via Seizure Protein 6. Biol Psychiatry. 2018;83:428-37.
44. Das B, Singh N, Yao AY, Zhou J, He W, Hu X, et al. BACE1 controls synaptic function through modulating release of synaptic vesicles. Mol Psychiatry. 2021;26:6394-410.
45. Lasztoczi B Klausberger T. Layer-specific GABAergic control of distinct gamma oscillations in the CA1 hippocampus. Neuron. 2014;81:1126-39.
46. Dominguez D, Tournoy J, Hartmann D, Huth T, Cryns K, Deforce S, et al. Phenotypic and biochemical analyses of BACE1- and BACE2-deficient mice. J Biol Chem. 2005;280:30797-806.
47. Kim DY, Carey BW, Wang H, Ingano LA, Binshtok AM, Wertz MH, et al. BACE1 regulates voltage-gated sodium channels and neuronal activity. Nat Cell Biol. 2007;9:755-64.
48. Sachse CC, Kim YH, Agsten M, Huth T, Alzheimer C, Kovacs DM, et al. BACE1 and presenilin/gamma-secretase regulate proteolytic processing of KCNE1 and 2, auxiliary subunits of voltage-gated potassium channels. FASEB J. 2013;27:2458-67.
49. Hessler S, Zheng F, Hartmann S, Rittger A, Lehnert S, Volkel M, et al. beta-Secretase BACE1 regulates hippocampal and reconstituted M-currents in a beta-subunit-like fashion. J Neurosci. 2015;35:3298-311.
50. Hartmann S, Zheng F, Kyncl MC, Karch S, Voelkl K, Zott B, et al. beta-Secretase BACE1 Promotes Surface Expression and Function of Kv3.4 at Hippocampal Mossy Fiber Synapses. J Neurosci. 2018;38:3480-94.
51. Huth T, Schmidt-Neuenfeldt K, Rittger A, Saftig P, Reiss K Alzheimer C. Non-proteolytic effect of beta-site APP-cleaving enzyme 1 (BACE1) on sodium channel function. Neurobiol Dis. 2009;33:282-9.
52. Du J, Zhang L, Weiser M, Rudy B McBain CJ. Developmental expression and functional characterization of the potassium-channel subunit Kv3.1b in parvalbumin-containing interneurons of the rat hippocampus. J Neurosci. 1996;16:506-18.

53. Kuhn PH, Koroniak K, Hogl S, Colombo A, Zeitschel U, Willem M, et al. Secretome protein enrichment identifies physiological BACE1 protease substrates in neurons. EMBO J. 2012;31:3157-68.
54. Song JY, Ichtchenko K, Sudhof TC Brose N. Neuroligin 1 is a postsynaptic cell-adhesion molecule of excitatory synapses. Proc Natl Acad Sci U S A. 1999;96:1100-5.
55. Budreck EC, Kwon OB, Jung JH, Baudouin S, Thommen A, Kim HS, et al. Neuroligin-1 controls synaptic abundance of NMDA-type glutamate receptors through extracellular coupling. Proc Natl Acad Sci U S A. 2013;110:725-30.
56. Wu X, Morishita WK, Riley AM, Hale WD, Sudhof TC Malenka RC. Neuroligin-1 Signaling Controls LTP and NMDA Receptors by Distinct Molecular Pathways. Neuron. 2019;102:621-35 e3.
57. Peixoto RT, Kunz PA, Kwon H, Mabb AM, Sabatini BL, Philpot BD, et al. Transsynaptic signaling by activity-dependent cleavage of neuroligin-1. Neuron. 2012;76:396-409.
58. Suzuki K, Hayashi Y, Nakahara S, Kumazaki H, Prox J, Horiuchi K, et al. Activity-dependent proteolytic cleavage of neuroligin-1. Neuron. 2012;76:410-22.
59. Polepalli JS, Wu H, Goswami D, Halpern CH, Sudhof TC Malenka RC. Modulation of excitation on parvalbumin interneurons by neuroligin-3 regulates the hippocampal network. Nat Neurosci. 2017;20:219-29.
60. Donato F, Rompani SB Caroni P. Parvalbumin-expressing basket-cell network plasticity induced by experience regulates adult learning. Nature. 2013;504:272-6.
61. Kim Y Spruston N. Target-specific output patterns are predicted by the distribution of regular-spiking and bursting pyramidal neurons in the subiculum. Hippocampus. 2012;22:693-706.
62. Graves AR, Moore SJ, Bloss EB, Mensh BD, Kath WL Spruston N. Hippocampal pyramidal neurons comprise two distinct cell types that are countermodulated by metabotropic receptors. Neuron. 2012;76:776-89.
63. Levinson JN El-Husseini A. Building excitatory and inhibitory synapses: balancing neuroligin partnerships. Neuron. 2005;48:171-4.
64. Li Y, Zhu K, Li N, Wang X, Xiao X, Li L, et al. Reversible GABAergic dysfunction involved in hippocampal hyperactivity predicts early-stage Alzheimer disease in a mouse model. Alzheimers Res Ther. 2021;13:114.

Figures

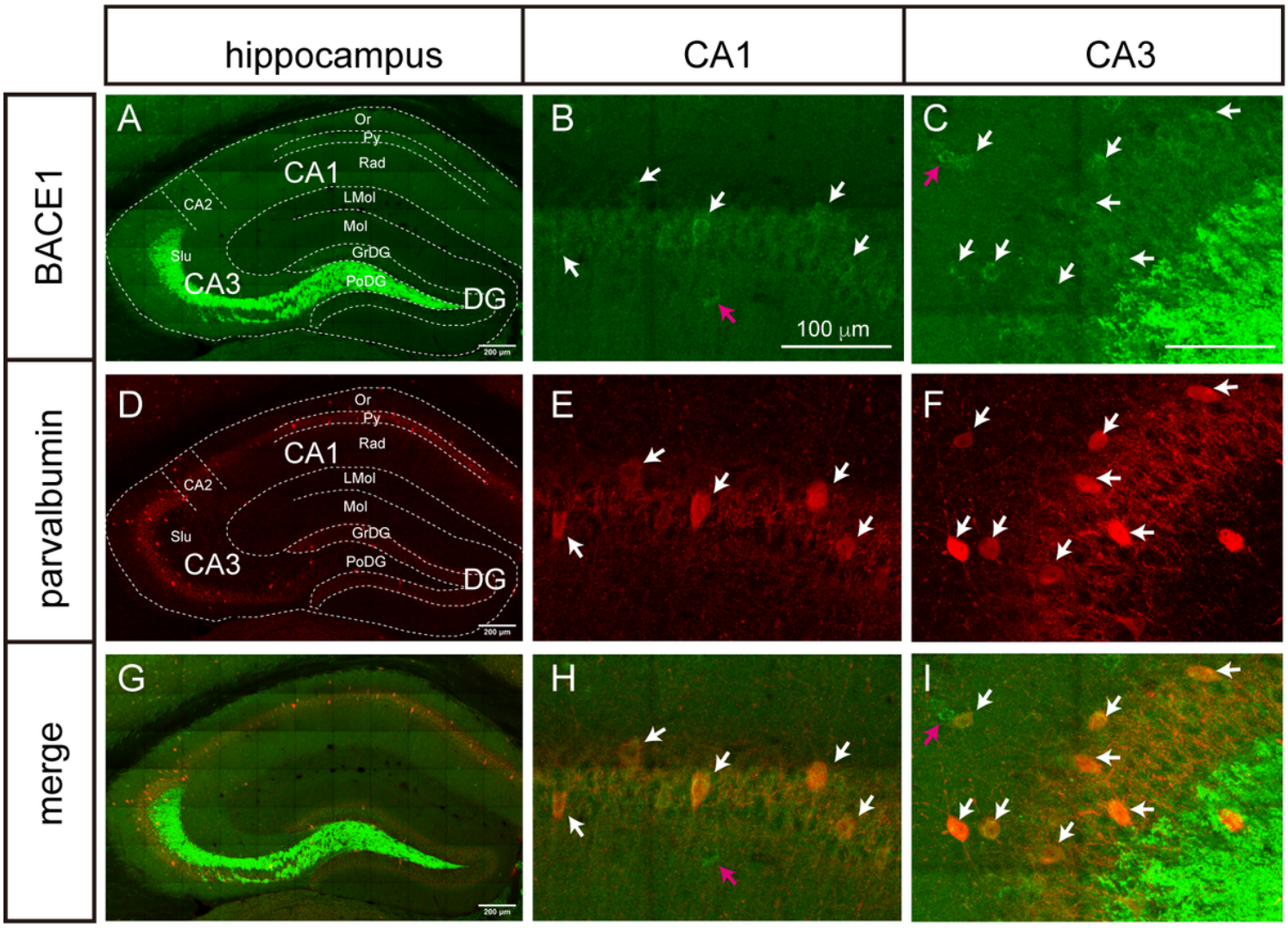

Figure 1

BACE1 is highly expressed in the parvalbumin interneuron of hippocampal CA1. The ten weeks old wild type mouse was subjected to double immunostaining with anti-BACE1 (green) and anti-parvalbumin (red) antibodies. **A, D, G,** the whole hippocampus was observed and captured by confocal microscopy. The selected CA1 (**B, E, H**) and CA3 (**C, F, I**) regions were enlarged. Scale bar, 200 mm in A, D, G; 100 mm in B-C, E-F, H-I. White arrows indicate parvalbumin-positive neurons with high expression of BACE1; purple arrows indicate neurons expressing BACE1 but not parvalbumin.

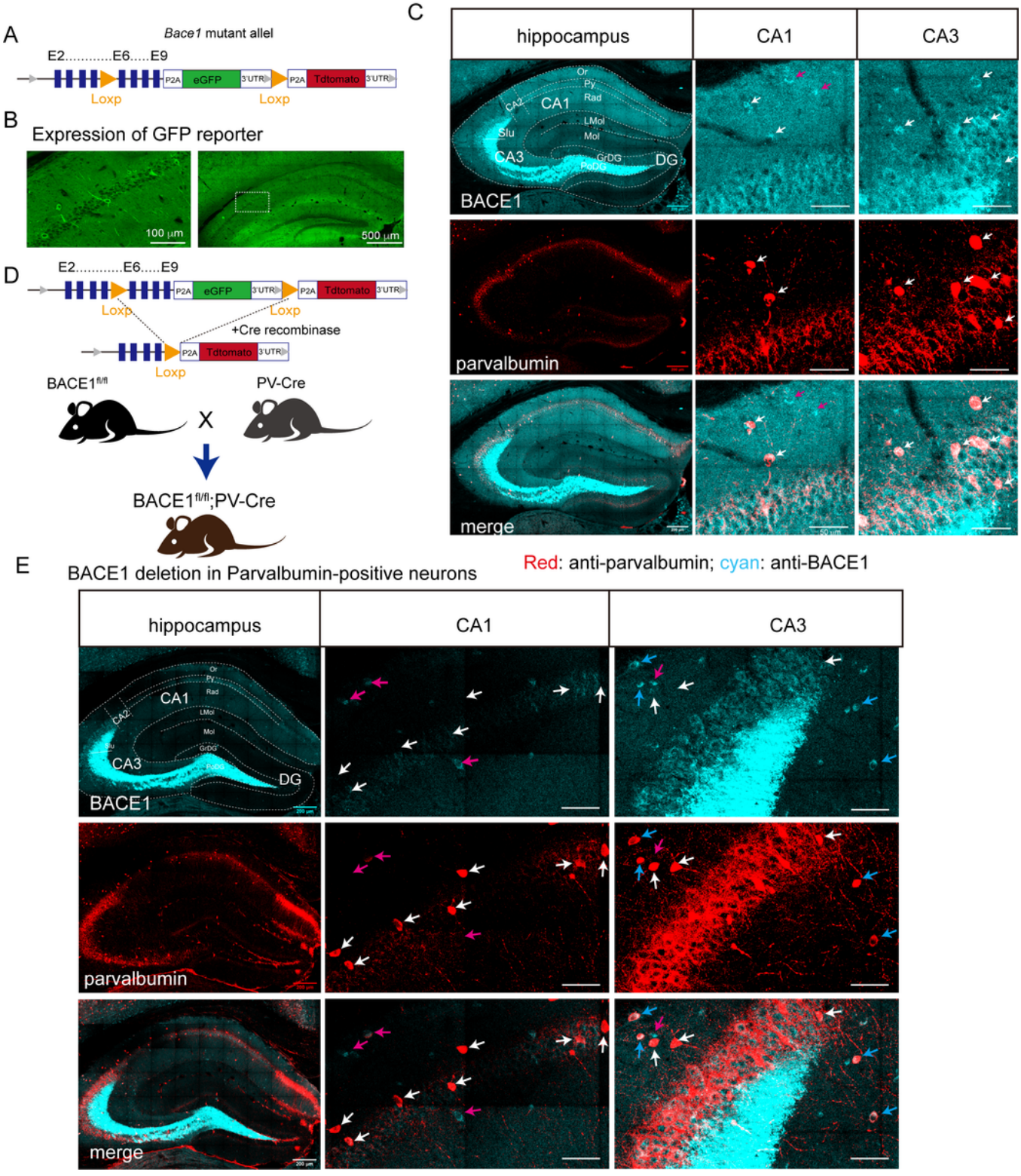

Figure 2

Establishment of conditional knockout mice with BACE1 deletion in parvalbumin neurons. A, schematics of the *loxp*-flanked (flox) targeting vector for BACE1 mutant allele. **B,** mouse brain expressing the BACE1 mutant allele can be identified by GFP reporter driven by endogenous *Bace1* promoter. The figure on the left is the enlargement from the dotted box of the figure on the right. Scale bar is 100 mm, and 500 mm, respectively. **C,** immunofluorescent staining of BACE1$^{fl/fl}$ mouse brain with anti-BACE1 and anti-

parvalbumin antibodies. The fluorescent conjugated secondary antibodies (cyan: Alexa fluor 647 for BACE1; red: Alexa fluor 594 for parvalbumin). White arrows indicate the parvalbumin-positive neuron with high expression of BACE1, while purple arrows show non-PV neurons but with BACE1 expression. **D,** schematics of generation of the mouse with BACE1 deletion in Parvalbumin neurons (BACE1$^{fl/fl}$;PV-Cre) in a Cre recombinase-dependent manner. **E,** expression of BACE1 and parvalbumin was detected in BACE1$^{fl/fl}$;PV-Cre mouse hippocampus and the CA1 and CA3 were enlarged from the whole image of the hippocampus. White arrows indicate parvalbumin-positive neurons (red) without expression of BACE1; purple arrows indicate neurons expressing BACE1 but not parvalbumin (cyan); blue arrows indicate neurons expressing both BACE1 and parvalbumin (red and cyan merged). Scale bar: 200 mm in the whole image of the hippocampus of C and E; 50 mm in CA1 and CA3 of C and E.

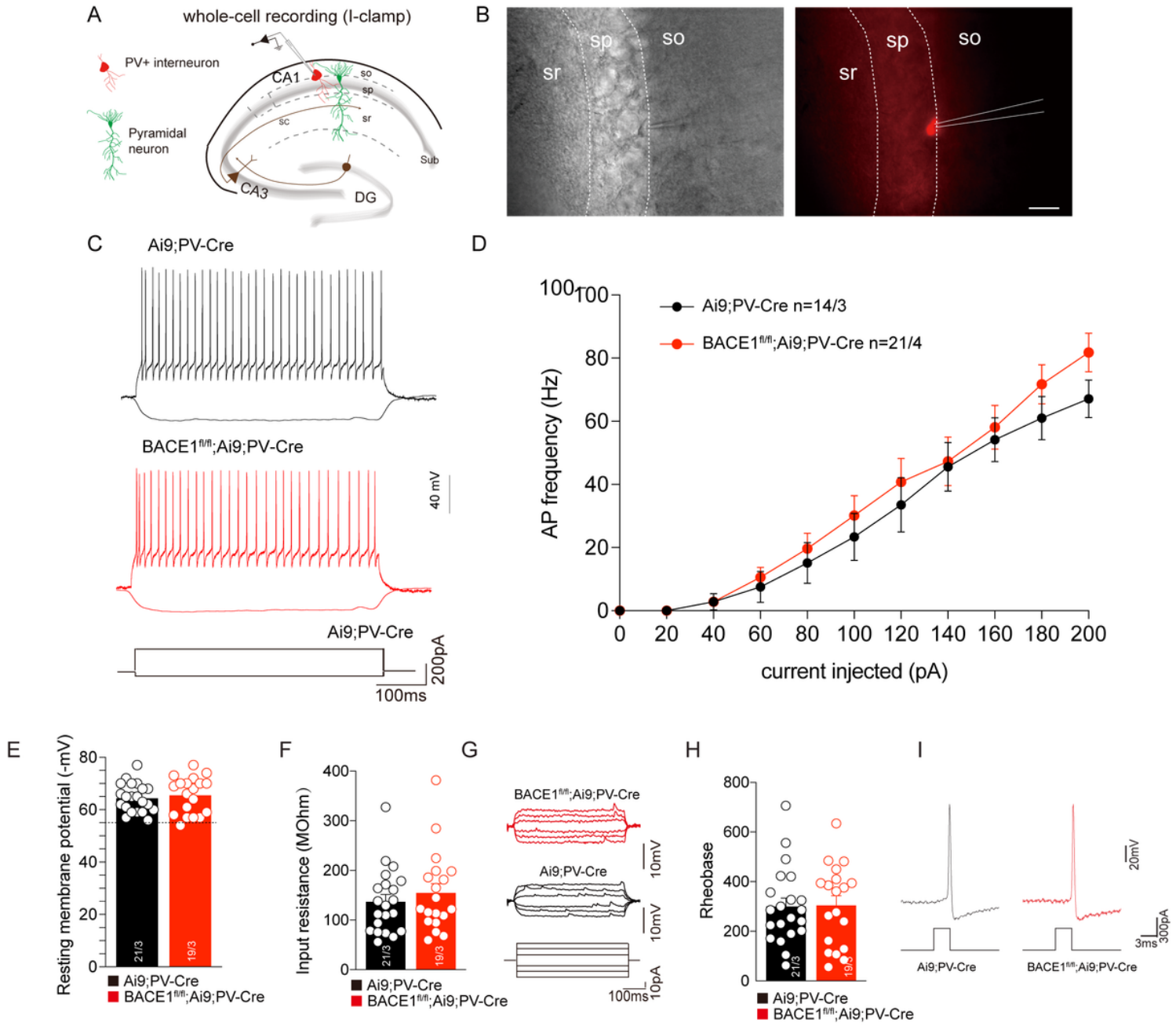

Figure 3

BACE1 deletion did not change the electrophysiological properties of CA1 PV INs. A, schematic diagram of whole-cell recording for PV INs. so, stratum oriens; sp, stratum pyramidale; sr, stratum radiatum; sc, Schaffer collateral; **B,** light (left) and fluorescent (right) microscope image of a recorded PV IN identified by Tdtomato expression. Scale bar, 20 mm. The dashed double-line represents a recording electrode. **C,** representative traces of action potential (APs) of CA1 PV INs in response to 500ms-long step currents in Ai9;PV-Cre and BACE1$^{fl/fl}$;Ai9;PV-Cre mice. **D,** plots of AP frequency against current injections. **E,** the resting membrane potential of recorded neurons. **F,** the input resistance of CA1 PV INs from Ai9;PV-Cre and BACE1$^{fl/fl}$;Ai9;PV-Cre mice was calculated by Ohm's law from **G,** subthreshold stimulation of current injections from -30 to +30 pA in the duration of 500 ms. **H,** step current injections (increment: 10 pA) crossing threshold was performed to determine neurons' short pulse (3 ms) rheobase. **I,** representative traces of the first firing triggered by suprathreshold current injection. The "n" and dots indicate individual neurons recorded, and data are presented as mean ± SEM. In D, two-way ANOVA analysis followed by Bonferroni's multiple comparisons test was used to compare the two groups. E, H, unpaired t-test, and F, Mann-Whitney test was used.

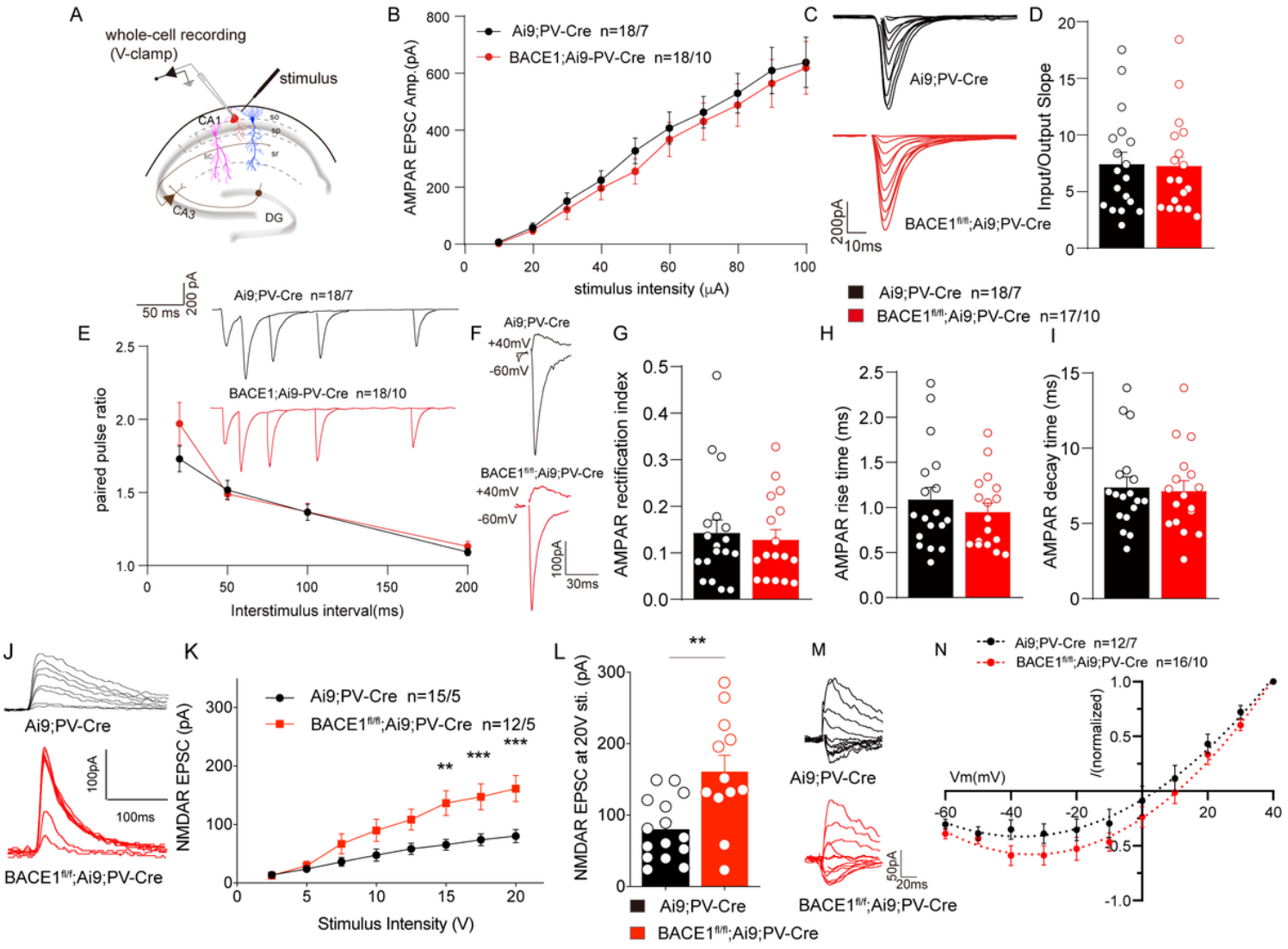

Figure 4

The CA1 PV INs with BACE1 deletion received a normal AMPAR-, but an enhanced NMDAR-mediated excitatory transmission. A, schematic diagram of stimulus-response of CA1 PV INs. The stimulating electrode was placed in stratum oriens (so) to evoke monosynaptic EPSCs on PV interneurons. **B,** analysis of input-output (I-O) relationship between AMPAR EPSCs and incremental stimulus intensities (in μA) 10, 20, 30, 40, 50, 60, 70, 80, 90, 100. **C,** representative traces of AMPAR-EPSCs on PV interneurons in Ai9;PV-Cre, and $BACE1^{fl/fl}$;Ai9;PV-Cre mice. **D,** bar graph of input/output slope of each cell. **E,** representative traces (inset) and plot showing paired-pulse ratio (PPRs) at interstimulus intervals of 20, 50, 100, and 200 ms with two-way ANOVA analysis followed by Bonferroni's multiple comparisons test. **F,** representative traces of AMPAR-EPSCs recorded at -60mV and +40 mV sequentially. **G,** the AMPAR rectification index was calculated as a ratio of EPSC at +40 mV to that at -60 mV. **H, I,** bar graph showing rise time, and decay time of AMPAR-EPSCs. **J,** representative traces of NMDAR-EPSCs recorded at +40 mV on CA1 PV INs. **K,** analysis of input-output (I-O) relationship between NMDAR-EPSCs and incremental stimulation intensities (in V) 2.5, 5.0, 7.5, 10.0, 12.5, 15.0, 17.5, 20.0, with two-way ANOVA analysis followed by Bonferroni's multiple comparisons tests, $^{**}p<0.01$, $^{***}p<0.001$ vs. Ai9;PV-Cre. **L,** the NMDAR-EPSC amplitude upon 20 V stimulation was analyzed by the unpaired t test with Welch's correction, $^{**}p = 0.0051$. **M,** representative traces of NMDAR-EPSCs at holding membrane potential from -60 to +40 mV in a step voltage of 10 mV. **N,** current-voltage (I-V) relationship of NMDAR-EPSCs of PV INs with two-way ANOVA analysis followed by Bonferroni's multiple comparisons test. The "n" and dots indicate neurons/mice.

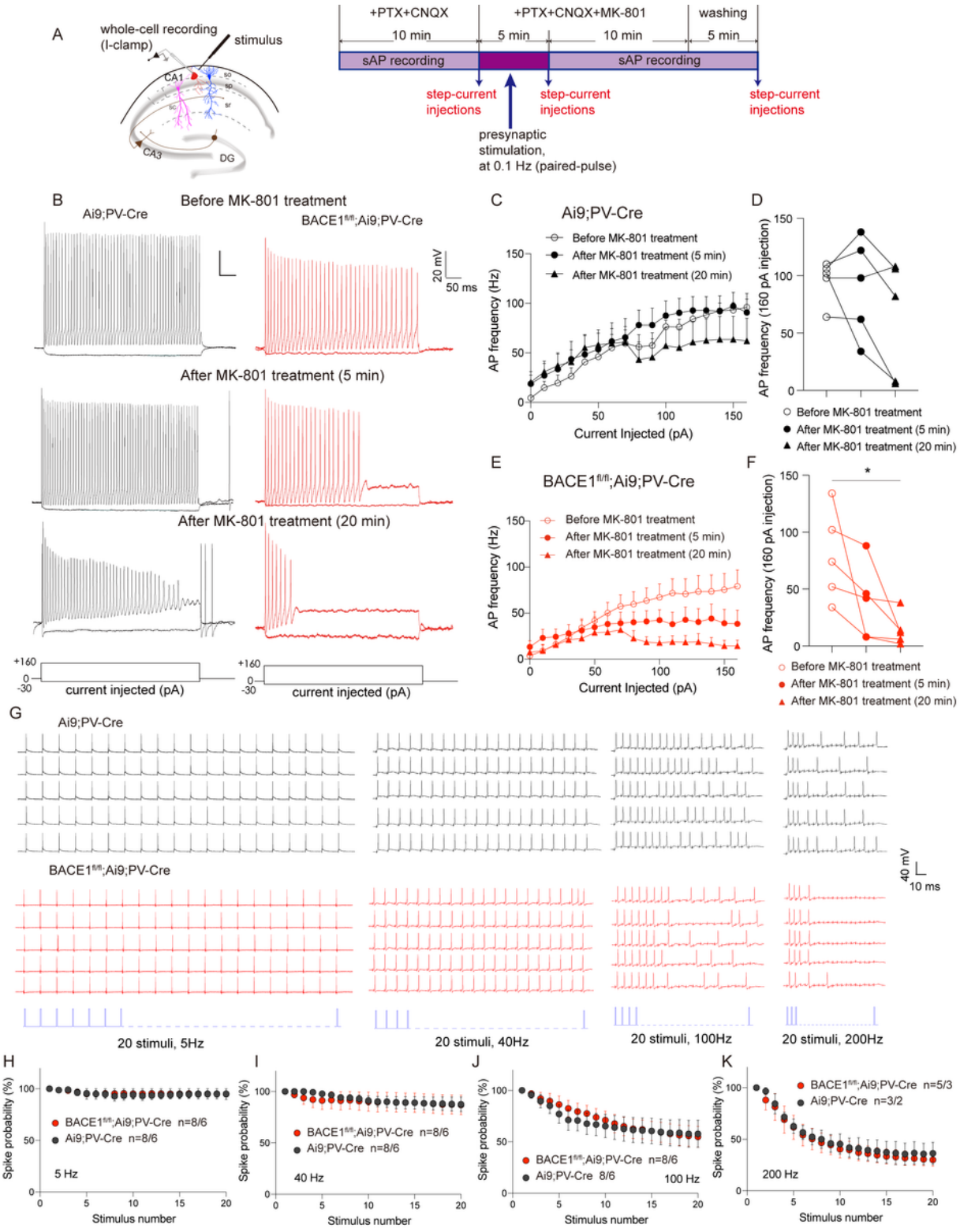

Figure 5

BACE1 deletion made MK-801 a greater degree of blockade with NMDARs but left intact the reliability in synaptic integration of CA1 PV INs. A, schematic diagram of whole-cell current-clamp recording under presynaptic electrode stimulation and drug treatment. **B,** typical traces of APs under step-current injections in CA1 PV INs from Ai9;PV-Cre mice (left column) and BACE1$^{fl/fl}$;Ai9;PV-Cre mice (right column) before and after treatment of MK-801. **C, E,** plots of AP frequency against current injections in Ai9;PV-Cre

cells (C) and BACE1$^{fl/fl}$;Ai9;PV-Cre cells (E). **D, F,** individual AP frequency of Ai9;PV-Cre cells (D) and BACE1$^{fl/fl}$;Ai9;PV-Cre cells (F) in response to current injection of 160 pA before and after MK-801 treatment. In C-F, paired t test was used, n = 5 pairs of neurons in Ai9;PV-Cre or in BACE1$^{fl/fl}$;Ai9;PV-Cre, *p = 0.0336. **G,** representative traces of evoked spikes upon repetitive presynaptic electrical stimulation at a frequency of 5, 40, 100, and 200 Hz. **H-K,** statistical plots of the probability of evoking spikes against prolonged stimulus trains in Ai9;PV-Cre and BACE1;Ai9;PV-Cre neurons for 5 Hz (H), 40 Hz (I), 100 Hz (J), and 200 Hz (K).

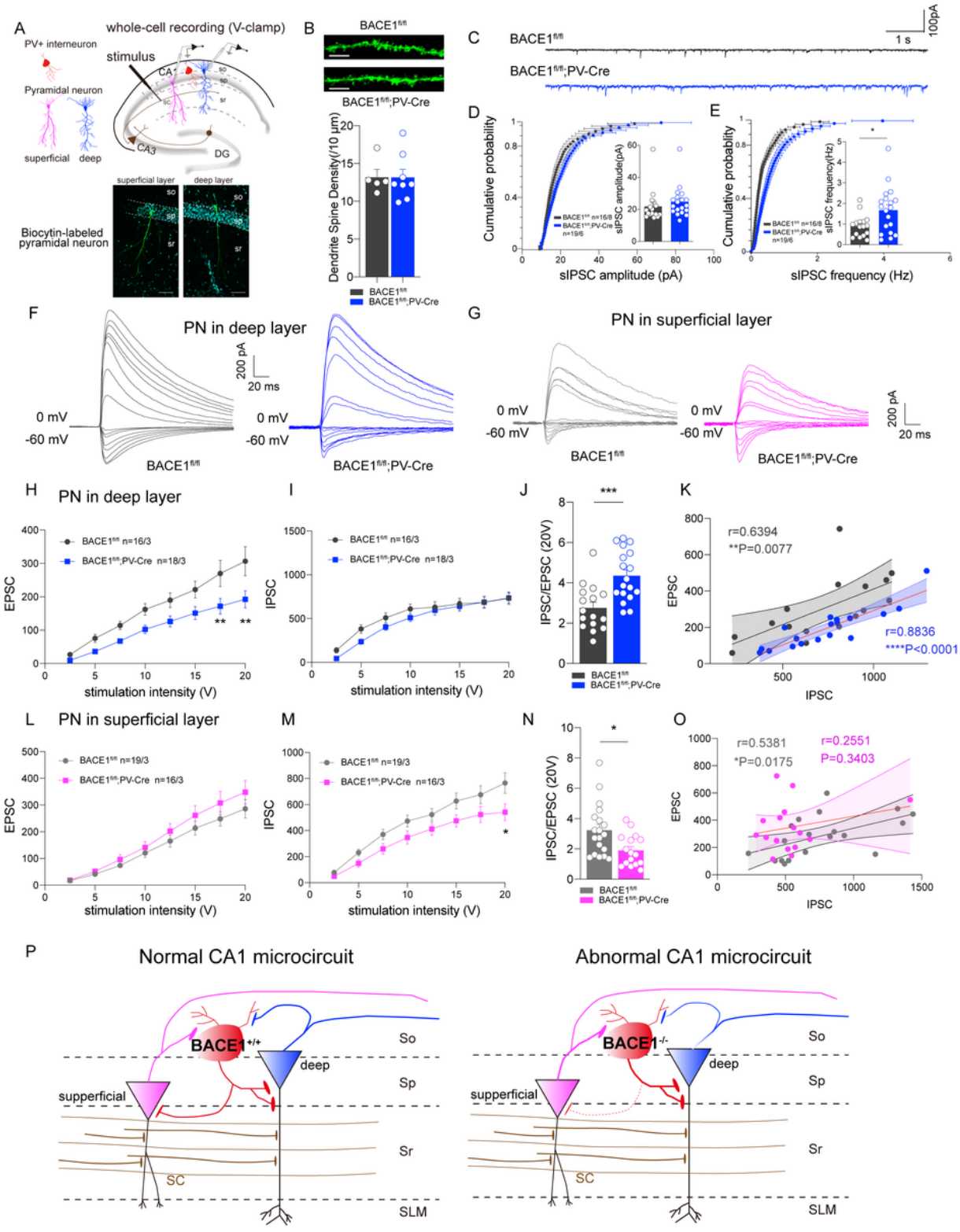

Figure 6

BACE1 deletion in PV INs reorganized the inhibitory/excitatory synaptic transmission on CA1 PNs in a non-uniform pattern.

A, schematic diagram of CA1 subpopulations and electrophysiological recording protocol (top) and biocytin-labeled neurons by recording pipette (below). Scale bar, 50 mm. **B,** representative dendrites of

CA1 pyramidal neuron labeled with biocytin (top) and statistical analysis of dendrites spine density per 10 mm (below). Scale bar, 5 mm. **C,** representative traces of spontaneous IPSC (sIPSC) from CA1 deep layer PNs of BACE1$^{fl/fl}$ and BACE1$^{fl/fl}$;PV-Cre mice. **D, E,** cumulative, and bar graph showing amplitude (D) and frequency (E) of sIPSC. The data were subjected to Mann-Whitney test (D) and Welch's t test (E), *p=0.0131. **F, G,** representative traces of evoked IPSCs (recorded at 0 mV) and EPSCs (recorded at -60 mV) in PNs located either in the deep layer (F) or superficial layer (G) of CA1. **H, I, L, M,** statistical analysis of evoked EPSCs (H, L) and IPSCs (I, M) from PNs in the deep layer (H, I) or superficial layer (L, M) under incremental stimulations (V): 2.5, 5, 7.5, 10, 12.5, 15, 17.5, 20, with theta glass electrode. **J, N,** bar graph showing IPSC/EPSC ratios from PNs in the CA1 deep layer (J) and superficial layer (N) under stimulus strength of 20 V. **K, O,** scatter diagram with linear regression of IPSC/EPSC in CA1 PNs in the deep layer (K) and superficial layer (O), respectively. The r and p values were determined by Pearson correlation. **P,** a proposed working model of BACE1 involvement in the homeostasis of CA1 local microcircuit mediated by PV INs. Two-way ANOVA followed by Bonferroni's multiple comparisons test was used in statistical analysis for H, I, L, M. In J, N, data were subjected to unpaired t-tests. *p < 0.05, **p < 0.01, ***p < 0.001 vs. BACE1$^{fl/fl}$. All neurons used in the analysis (H-O) were from 3 pairs of mice.

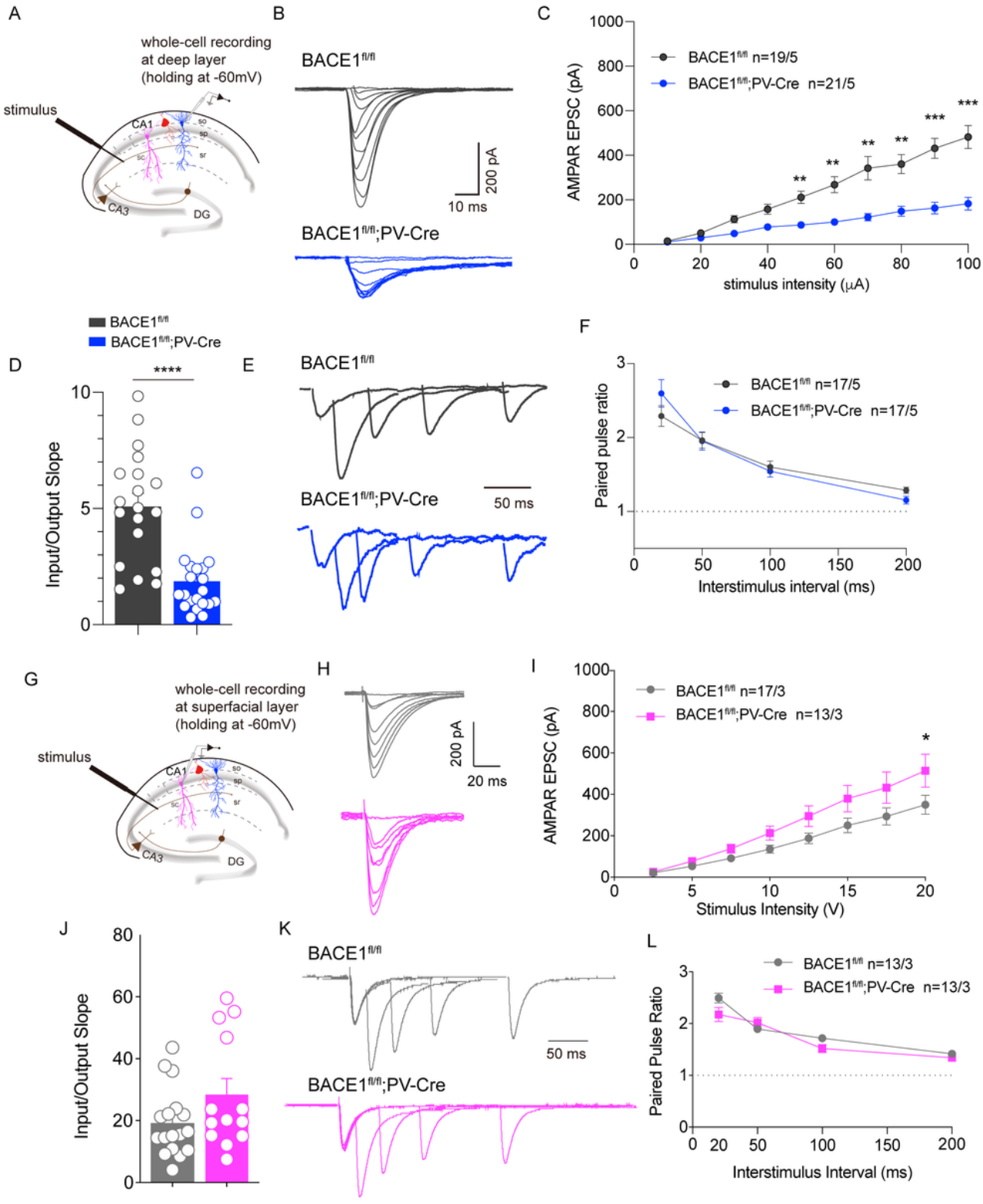

Figure 7

The BACE1 deletion in PV INs resulted in distinct responses of CA1 PNs to synaptic transmission in SC-CA1 long projection. A, G, schematic of whole-cell current recording of CA1 deep layer PNs (A) or superficial layer PNs (G) in response to SC stimulation. **B, H,** representative traces of AMPAR-EPSCs on CA1 deep layer PNs (B) or superficial layer PNs (H) in BACE1$^{fl/fl}$ and BACE1$^{fl/fl}$;PV-Cre mice. **C, I,** analysis of input-output (I-O) relationship between AMPAR EPSCs and incremental stimulation intensities (C, in μA

with mental electrode; I, in V with theta glass electrode), with two-way ANOVA analysis followed by Bonferroni's multiple comparisons test, *$p < 0.05$, **p < 0.01, ***$p < 0.001$ vs. BACE1$^{fl/fl}$. **D, J,** input/output slope of each cell was calculated and analyzed with the Mann-Whitney test, ****p <0.0001. **E, F, K, L,** representative traces and plots showing paired-pulse ratio (PPRs) of CA1 deep layer PNs (E, F) or superficial layer PNs (K, L) at interstimulus intervals of 20, 50, 100, and 200 ms with two-way ANOVA analysis followed by Bonferroni's multiple comparisons test. The "n" and dots indicate neurons/mice.

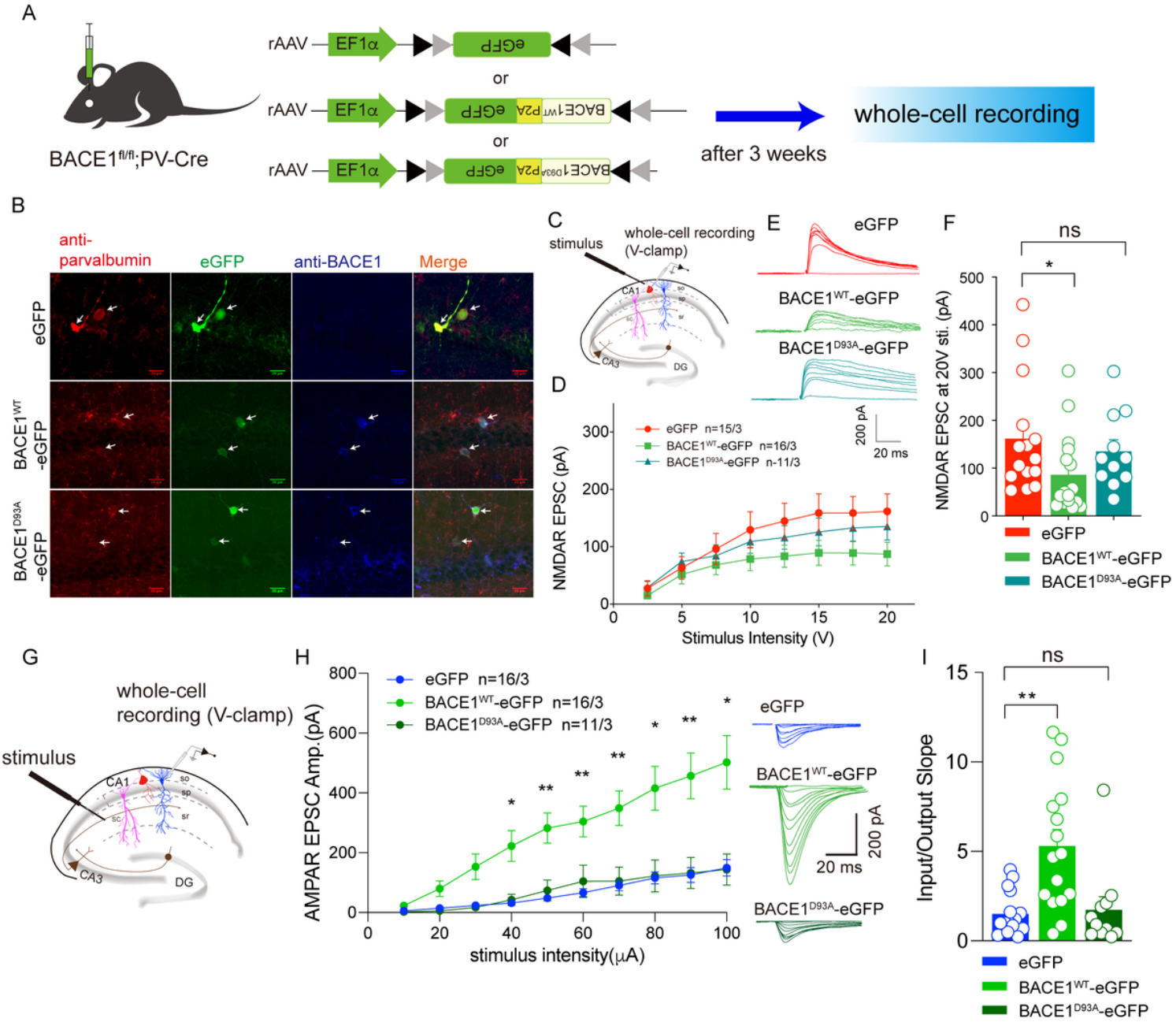

Figure 8

Specific local recovery of BACE1 expression rescued the NMDAR EPSC in PV INs and AMPAR EPSC in CA1 deep layer PNs in an enzymatic-dependent manner. A, diagram of experiment on injection of recombinant adeno-associated virus (rAAV) carrying eGFP- or BACE1^{WT}-P2A-eGFP- or BACE1^{D93A}-P2A-

eGFP-DIO driven by EF1a promoter into BACE1$^{fl/fl}$;PV-Cre mouse hippocampal CA1. The mouse slices were prepared three weeks later, and a whole-cell recording was performed. **B,** the infected cells were identified by eGFP and immunostaining with anti-parvalbumin and anti-BACE1 antibodies. Bar scale: 20 μm. **C,** schematic diagram of voltage-clamp whole-cell recording of PV INs. **D,** analysis of input-output (I-O) relationship between NMDAR-EPSCs and incremental stimulus intensities (in V) 2.5, 5, 7.5, 10, 12.5, 15, 17,5, 20, with two-way ANOVA analysis followed by Bonferroni's multiple comparisons test. **E,** representative traces of the evoked NMDAR EPSCs on PV INs expressing eGFP, BACE1^{WT}-eGFP, and BACE1^{D93A}-eGFP, respectively. **F,** bar graph showing the amplitude of evoked NMDAR EPSC on PV INs under 20 V stimulus intensity. **G,** schematic diagram of voltage-clamp whole-cell recording of CA1 deep layer PNs. **H,** input-output (I-O) relationship between AMPAR EPSCs amplitude and incremental stimulation intensities (in μA) 10, 20, 30, 40, 50, 60, 70, 80, 90, 100, with two-way ANOVA analysis followed by Bonferroni's multiple comparisons test, *$p < 0.05$, **$p < 0.01$ vs. eGFP. The inset shows representative traces of AMPAR-EPSCs in CA1 PNs of BACE1$^{fl/fl}$;PV-Cre mice injected with AAV-DIO-eGFP or AAV-DIO-BACE1^{WT}-P2A-eGFP or AAV-DIO-BACE1^{D93A}-P2A-eGFP. **I,** input/output slope of each cell was calculated and analyzed. The Kruskal-Wallis test was used in F and I, BACE1^{WT}-eGFP vs. eGFP, *p = 0.0283, **p = 0.0064, ns: no significance. The "n" indicates neurons/mice.

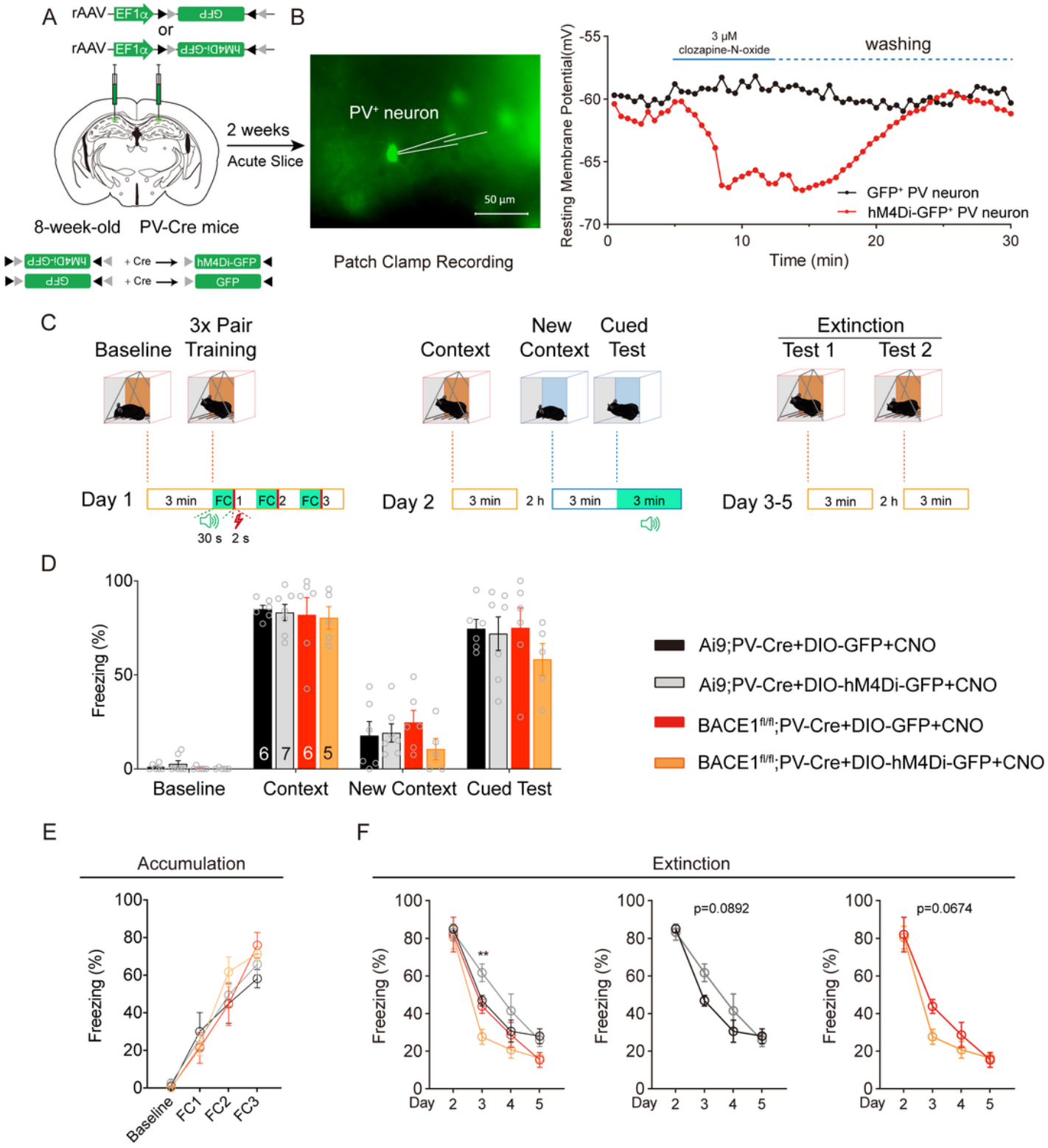

Figure 9

BACE1 deletion in CA1 PV INs reset the priming of fear memory extinction. A, schematic of stereotactic injection of AAV virus-carrying DIO-hM4Di-GFP or DIO-GFP in hippocampus CA1. **B,** Left, microscopy of patch-clamp setup showing fluorescence image of a hM4Di-GFP expressing neuron in the hippocampal slice. Right, the continuous membrane potential recording of GFP- or hM4Di-GFP expressing neuron before and after CNO (3 μM) treatment. **C,** schematic diagram of protocols for contextual fear

conditioning and fear memory extinction. **D,** bar graph showing the percent of freezing time for animals (PV-Cre;Ai9, BACE1$^{fl/fl}$;PV-Cre, respectively, injected with AAV-DIO-GFP or AAV-DIO-hM4Di-GFP) in different episodes of a test, and all animals were treated twice one day with 10 mg/kg CNO 1 h before and 10 h after a test for all five days). Two-way ANOVA followed by Bonferroni's multiple comparisons test was used in statistical analysis. **E,** percent of freezing time during three rounds of fear conditioning (FC1-FC3). **F,** statistical analysis for averaged percent of freezing time during day 3-day 5 of fear extinction with two-way ANOVA followed by Bonferroni's multiple comparisons test, $^{**}p < 0.01$, PV-Cre;Ai9 expressing hM4Di vs. BACE1$^{fl/fl}$;PV-Cre expressing hM4Di. All data are presented as mean ± SEM, n = 6 mice for PV-Cre;Ai9 expressing GFP, n = 6 mice for BACE1$^{fl/fl}$;PV-Cre expressing GFP, n = 7 mice for PV-Cre;Ai9 expressing hM4Di, n = 5 mice for BACE1$^{fl/fl}$;PV-Cre expressing hM4Di.

Supplementary Files

This is a list of supplementary files associated with this preprint. Click to download.

- Statisticaldescription.xlsx
- Supplmentaryinformation.docx